

Optimization of hole transport layers for Cu₂FeSnS₄ solar cells via SCAPS-1D simulation: Investigating the impact of interface defects on practical efficiency limits

M.K. Jyolsna Raj ^a, Kallol Mohanta ^a, Sebin Devasia ^{a,b}, B. Geetha Priyadarshini ^{a,*}

^a Nanotechnology-Research Innovation and Incubation Centre (NRIIC), PSG Institute of Advanced Studies, Coimbatore, Tamil Nadu, 641004, India

^b Department of Physics, PSG Institute of Technology and Applied Research, Coimbatore, Tamil Nadu, 641062, India

ARTICLE INFO

Keywords:

Hole transport layers (HTL)
SCAPS simulation
Shallow acceptor densities
Interface defect density
Efficiency limits

ABSTRACT

The quaternary Cu₂FeSnS₄ (CFTS) chalcogenide garners significant interest as a sustainable alternative in solar cell applications due to its abundant and non-toxic composition. This study uses SCAPS-1D simulations to examine the performance of CFTS solar cells (ITO/HTL/CFTS (400 nm)/CdS (200 nm)/ZnO (10 nm)/Al) using three distinct hole transport layers (HTLs), namely NiO_x, Cu₂O, and CuI. The simulations led to a deeper understanding of their practical efficiency limits, considering the huge gap in the theoretical and experimental efficiency values reported earlier. The investigations reveal the precise mechanisms and the influence of hole transport layers on the device performance, specifically the bulk and interface defect densities. In addition, the other major aspects of CFTS solar cell performance, including the correlation between electric field, generation rate, and recombination rate are discussed. Our observations suggest that while identifying a suitable hole transport layer, it is imperative to consider these parameters, which are often overlooked in many numerical simulations, resulting in unrealistic theoretical efficiency values in contrast to the low efficiency observed in practical devices. Here, the optimized ITO/CuI/CFTS/CdS/ZnO/Al configuration demonstrated a maximum efficiency of 5.05 %, with a V_{oc} of 0.55 V, J_{sc} of 14.5 mA/cm², and FF of 61.8 %, which are in accordance with experimental values reported. Thus, the study here emphasizes the importance of considering the defect densities, electric field, generation rate, and recombination rate to bridge the gap between theoretical and practical efficiency values, which can significantly influence the design strategies to enhance the CFTS solar cell efficiency.

1. Introduction

The increasing global energy demands and the necessity of sustainable solutions drive the research in photovoltaic technology to achieve higher efficiency in low-cost devices fabricated using non-toxic materials. Over the past decade, quaternary chalcogenide materials, particularly kesterite-type, have garnered considerable attention due to their promising characteristics, including extrinsic p-type properties with an optimal band gap (1.2–1.8 eV), high absorption coefficients (1×10^{-4} cm⁻¹), and eco-friendly composition [1]. On the other hand, traditional quaternary materials such as CIGS, CdTe, and GaAs have also been prominent in thin-film photovoltaic technologies [2–5]. However, the transition to kesterite-type solar cells has been caused by the scarcity of Indium and Gallium, the limited availability of tellurium, and the toxicity of Cadmium.

1.1. Kesterite-type solar cells

Kesterite model solar cells, particularly CZTS solar cells, have demonstrated significant advancements, although their maximum efficiency remains relatively low, reaching approximately 15 %. Despite the potential for efficiencies up to 30 % according to the Shockley-Queisser limit, achieving such high efficiencies remains a challenge [6]. Copper-based chalcogenide has shown significant potential as a superior alternative to carbon-based renewable energy sources. Chalcogenide Cu₂FeSnS₄ (CFTS), which is composed of copper, iron, tin, and sulfur, has attracted interest for photovoltaic applications because of its energy band gap between 1.2 and 1.6 eV and an optical coefficient over 10⁴ cm⁻¹ [7–11]. The most widely used crystal structure of CFTS is tetragonal stannite, with I-42m space group, with $a = b = 5.46$ Å and $c = 10.72$ Å represented in Fig. 1. Among these quaternary materials, CFTS

* Corresponding author.

E-mail address: bgp@psgias.ac.in (B. Geetha Priyadarshini).

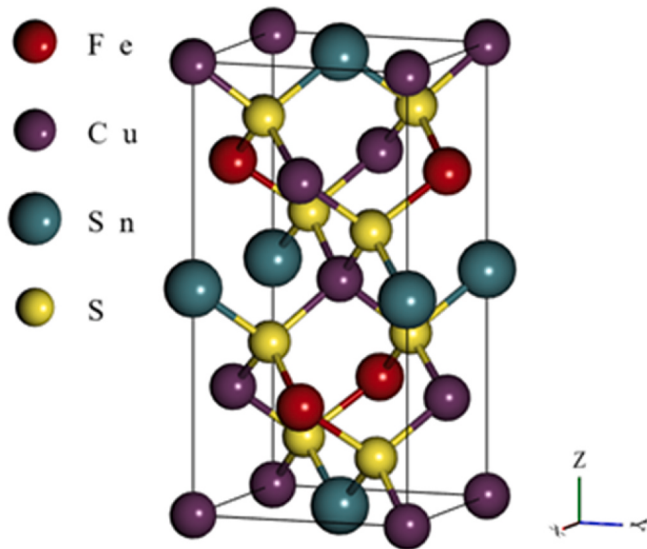


Fig. 1. Stannite structure of $\text{Cu}_2\text{FeSnS}_4$.

has emerged as a versatile material with applications ranging from solar cells to photo-electrodes in DSSCs [7,12–15], memory switching [16], and more [10,11,17,18]. Various numerical studies on CFTS solar cells have explained the device's performance based on different device parameters [19–23]. The highest reported efficiency for a CFTS solar cell is 2.9 % which has a device structure of ITO/Cu@-NiO/CFTS/Bi₂S₃/ZnO/Al fabricated through a solution-based process [13]. Here, Cu-doped NiO played a key role as the hole transport layer, while ZnO acted as an electron transport layer. The success of this design may be due to the unique electrical and structural properties of Cu as a dopant, which improved the integration of the hole transport layer, paving the way for further advancements in CFTS solar cell technology. The study's primary goal is to better understand the impact of hole transport layers and improve the CFTS solar cell efficiency while considering practical limitations.

The carrier lifetime, measured in seconds (τ), denotes the average time required for a minority carrier to recombine, which significantly influences the performance of photovoltaic cells. In the fabrication of photovoltaic cells, the minority carrier lifetime stands as a crucial parameter for solar cell characterization. It is intricately linked to the recombination rate, expressed as

$$\tau = \frac{\Delta n}{R} \quad (1)$$

Where ' τ ' represents the minority carrier lifetime, 'R' signifies the recombination rate, and ' Δ ' denotes the excess minority carrier concentration.

1.2. Hole transport layers in kesterite solar cells

Proper selection of the hole transport layer (HTL) can mitigate the rollover effect, lower the barrier height of the back contact, and minimize recombination losses of minority carriers at the back contact [24, 25]. The primary role of HTL is to extract holes from the absorber layer and transfer them to the appropriate electrodes, so it is critical to comprehend the practical implications of selecting hole transport layers. Nickel oxide (NiO_x) materials are frequently used in perovskite-based devices, CdTe, and organic solar cells due to their p-type characteristics, high transmittance, and wide band gap of 3.5–3.9 eV. Their band structure aligns well with band edge levels of CZTS/CZTSe-type materials, minimizing recombination losses and enhancing charge carrier separation and transport which results in better open-circuit voltage and overall power conversion efficiencies. Besides, NiO_x offers advantages

such as high conductivity, chemical stability, flexibility, high storage capacity, and low cost [26–30]. Similarly, cost-effective and eco-friendly Cu_2O exhibits high hole mobility and good band alignment for p-type quaternary chalcogenide absorber layers such as CZTS. The performance of oxide thin films can be enhanced by employing suitable deposition techniques. Incorporating oxide buffer layers such as Cu_2O and NiO_x reduces carrier recombination and serves as an efficient electron-blocking layers by introducing an intermediate energy band that promotes hole extraction and transport. Furthermore, the chemical stability of these oxides helps protect the underlying CFTS layer from oxidation. These are more resilient to environmental deterioration than organic buffer layers. NiO_x and Cu_2O have been deposited using sputtering methods, especially as it is used as the hole transport layers for chalcogenide solar cells, organic solar cells, as well as perovskite solar cells [29–32]. Numerous reports describe the utilization of RF and DC sputtering to produce thin films using NiO_x and Cu_2O , which will provide good adhesion and allow for appropriate tuning [33]. Oxide thin films are deposited by regulating the development conditions by maximizing appropriate variables such as oxygen partial pressures, temperatures, and deposition rates.

Their suitable valence band position, which aligns well with the CZTS layer reduces the energy barrier, facilitating effective hole extraction and lower interface recombination to yield enhanced power conversion efficiency [34]. This alignment enhances photovoltaic performance by minimizing energy and recombination losses at interfaces. Similarly, the cheap and non-toxic p-type CuI semiconductor has a larger band gap of 3.1 eV, offering excellent optical transmittance of 86 %, low cost, eco-friendliness, low extinction coefficient, and high hole mobility (0.5–2 cm²/V·s) [26,34–36]. Importantly, it has an ideal band alignment with the CZTS absorber layer [34] for the fabrication of the CFTS solar cells. CuI is deposited via thermal evaporation, a technique that, when conducted under vacuum conditions, minimizes the risk of oxidation. This method enhances the adhesion of CuI to glass substrates, and subsequent post-annealing further mitigates defect formation and improves the stability of the CuI thin films. CuI has been used as a hole transport layer in kesterite solar cells as well as perovskite solar cells, which improved the performance of photovoltaic devices [31,37–40].

Therefore, in this study, NiO_x , CuI, and Cu_2O were selected as suitable HTL materials to investigate their impact on the performance of CFTS solar cells, as they are composed of non-toxic elements and encompass both oxide and non-oxide materials. This study aims to enhance the efficiency of CFTS solar cells by incorporating suitable HTL and addressing fabrication challenges. In particular, surface passivation and surface imperfections due to material composition, and the presence of impurities, which also show deviation from the stoichiometry of CFTS, deposition temperature, as well as humidity, affect the fabrication process, which deteriorates the performance of CFTS solar cells. This detailed analysis ensures that potential defects and their impacts on device performance are accounted for, providing a realistic assessment of the solar cell's efficiency and reliability. The SCAPS-1D simulation framework relies on several simplifying assumptions, notably that all absorber layers are laterally homogeneous and free of structural defects. It does not account for lateral carrier transport or material inhomogeneities. Conductive secondary phases like Cu_2S , which could create shunting paths due to their unique electronic characteristics, are excluded from the model [41,42]. Instead, it assumes a uniform single-phase material with no representation of secondary phase geometry or interfacial effects. Defect states are considered to be evenly distributed throughout each layer, and interfaces are idealized, lacking interdiffusion, secondary phase formation, or potential drops caused by grain boundaries or conductive inclusions.

Similar efforts in CZTS-based solar cells have shown performance improvements [34,35], prompting further investigation into the impact of HTL on CFTS-based solar cells and their potential to increase efficiency using numerical simulations [35].

1.3. SCAPS-1D simulations

SCAPS-1D is a one-dimensional simulator developed by Mac Burgelman and colleagues, specifically designed for solar cell devices with multiple layers [43]. It requires an input of electrical and optical parameters under optimal conditions to achieve accurate simulations. SCAPS-1D facilitates the analysis of device performance by altering factors such as interface defect density, charge carrier densities, electron affinity, band gap, thickness, and shallow donor and acceptor densities [44–47]. As given in Table 1, SCAPS-1D software has been efficiently utilized to predict the performance parameters of various photovoltaic devices, especially chalcogenide and halide solar cells.

The software numerically solves the one-dimensional Poisson's and continuity equations, which include free electrons and holes.

$$\frac{d}{dx} \left(\epsilon_0 \epsilon \frac{d\Psi}{dx} \right) = -q \left(p - n + N_D^+ - N_A^- + \frac{\rho_{\text{def}}}{q} \right) \quad (2)$$

$$-\frac{\partial J_n}{\partial x} - U_n + G = 0 \quad (3)$$

$$-\frac{\partial J_p}{\partial x} - U_p + G = 0 \quad (4)$$

where 'n' and 'p' stand for electron and hole concentration, respectively, and ' Ψ ' for electrostatic potential. Ionized donor and acceptor densities are represented by N_D^+ and N_A^- , respectively. ' J_n ' and ' J_p ' are the electron and hole current densities, 'G' is the generation rate, and 'U' indicates the recombination. The HTL thicknesses predominantly affect the charge density distribution (ρ) and electrostatic potential (ψ), which in turn modify the electric field within the device. Furthermore, the choice of HTL materials affects the shallow acceptor density in Poisson's equation by modifying the charge density (and electrostatic potential). Similarly, the generation rate of electron-hole pairs $G(\lambda, x)$ can be calculated in SCAPS-1D software with total photon flux, $N(\lambda, x)$, using equation (5),

$$G(\lambda, x) = \alpha(\lambda, x) \cdot N(\lambda, x) \quad (5)$$

In addition, the HTL influences the carrier dynamics, recombination rate, and interface quality, which collectively determine the shallow acceptor density contribution to the overall electrostatic characteristics of the solar cell.

- i) HTL thickness: HTL thickness directly affects the charge transport dynamics and carrier recombination within the solar cell
- ii) Shallow acceptor density: Shallow acceptor levels above the valence band readily capture electrons, thereby increasing the concentration of mobile holes within the material.
- iii) Interface density: Interface density refers to the density of states at the interfaces between different layers in a solar cell device, which includes interface traps, defect states, and fixed charges, that can capture or release carriers, affecting the overall charge distribution.

iv) Series and Shunt Resistance: While series and shunt resistances are not directly part of Poisson's equation, they affect the electrical behavior and boundary conditions in device simulations. High series resistance causes voltage drops and uneven carrier distribution, while low shunt resistance leads to leakage currents, both altering charge density and potential profiles. Series resistance typically comes from contacts, semiconductors, and transparent electrodes, whereas shunt resistance represents unintended current pathways that degrade device performance when too low.

In addition, the electric field, generation rate and recombination rate can vary with the thickness of transport layers. Properly accounting for these parameters in device simulations ensures accurate modeling of solar cell performance.

1.3.1. SCAPS-1D simulation for CFTS solar cells

Numerical studies, such as DFT [36,55], SETFOS [56,57] SCAPS-1D [19,21], WxAMPS [36,58], and SILVACO [22,23], provide insights into CFTS solar cell performance to explore the practical feasibility for device fabrication. As listed in Table 2, SCAPS-1D simulation software could theoretically predict the practical efficiency of CFTS solar cells. Many numerical simulations on CFTS and CZTS solar cells indicate that they can reach even higher efficiency levels. However, such efficiencies have not yet been achieved in practical devices. One major reason for this mismatch is the disregard of various factors, including bulk and interface defects, which can significantly drop the efficiency of kesterite-type solar cells. However, there aren't many reports that look into the limitations of efficiency drain and examine how defects in quaternary materials affect device performance. Only a few theoretical articles highlight the interface defects that result in trap states, which can lower

Table 2
CZTS and CFTS solar cell parameters from SCAPS-1D simulations.

Device Configuration	Performance parameters				Ref.
	V_{oc} (V)	J_{sc} (mA/cm ²)	FF (%)	Efficiency (%)	
Mo/CZTS/CdZnS/iZnO/ITO	0.621	41.01	78.54	19.57	[59]
Sapphire/a-Si:H/Ba (Zr _{0.95} Ti _{0.05})S ₃ /CdS/i-ZnO/AZO	1.03	31.05	56.2	17.89	[60]
ZnO:Al/i-ZnO/CdS/CZTS/Mo	0.64	32.96	83.75	25.72	[61]
Ni/Sb ₂ S ₃ /CZTS/WS ₂ /FTO/AI	0.90	24.94	86	25.71	[62]
Si/CZTS/CdS/In ₂ O ₃ /ZnO	0.71	24.93	66.62	11.89	[63]
FTO/ZnS/CZTS/variable HTLs/Au	1.19	32.05	83.37	31.86	[34]
FTO/TiO ₂ /CFTS/Mo	1.033	24.92	86.54	22.27	[19]
Mo/MoSSe/CZT(S,Se)/CdS/ZnO(i)/AZO/Al/MgF ₂	1.194	35.37	62.65	26.47	[64]
FTO/TiO ₂ /CFTS/Mo	0.9995	23.37	85.94	19.97	[20]

Table 1
SCAPS-1D software for the theoretical prediction of solar cell performance and experimental validation.

Device structure	Theoretical				Experimental				Ref.
	V_{oc} (V)	J_{sc} (mA/cm ²)	FF (%)	η (%)	V_{oc} (V)	J_{sc} (mA/cm ²)	FF (%)	η (%)	
ITO/ZnO/ZnS/CNTS/Cu ₂ O	1.03	6.44	69.27	4.6	0.75	6.82	53.1	2.71	[48]
CZTS/CdS/ZnO/ITO	0.37	13.14	37.9	1.93	0.38	13.32	41.92	2.18	[49]
CdS/CZTS Interface	0.61	17.58	59.45	6.41	0.61	17.90	62.00	6.77	[50]
ZnO:Al/i-ZnO/CdS/CZTS/Mo	0.66	19.5	57.48	8.4	0.61	19.5	65.8	8.4	[51]
ITO/i-ZnO/AZTS/CZTS/Mo	0.64	17.5	40	4.51	0.641	11.53	43.2	4.83	[52]
FTO/SnO ₂ /FAPbI ₃ /Spiro-OMeTAD	1.12	25.18	74.71	21.04	1.123	25.58	73.26	21.07	[53]
Perovskite/CIGS tandem solar cell	0.72	36.22	77.05	20.08	0.72	36.30	76.80	20.1	[54]

CFTS efficiency. The PCE values drop from 15 % to 4 % with the introduction of trap levels within bulk defect density and from 17 % to 2 % with the simultaneous introduction of interface trap density [22,23]. All this literature details the density of defect states, which encompasses several recombination processes, including Auger, Shockley-Read-Hall (SRH), and radiative, indicating a maximum efficiency drop of 14 % may be attributable to bulk defect densities [22].

Understanding the crucial interdependence among material and device parameters as well as their practical implications is crucial for pushing the boundaries of solar cell efficiency. The current work aims to address this gap by investigating the role of HTL in CFTS solar cells with ZnO as an ETL, utilizing SCAPS-1D simulation to provide detailed insights into their impact on device performance.

2. Device structure and simulation parameters

The architecture of the simulated CFTS solar cell includes various layers designed to optimize the conversion of light into electrical energy. The device parameters used for the simulation is shown in [Table 3](#) and [Table 4](#). The configuration used for the simulation is shown in [Fig. 2](#) and consists of the following layers:

- Back Contact: Indium Tin Oxide (ITO) is used as the back contact due to its high transparency and good electrical conductivity, allowing maximum light to reach the absorber layer while efficiently collecting electrons.
- Window Layer: Zinc oxide (ZnO) is a commonly used ETL due to its wide bandgap, good electron mobility, and stability. It facilitates efficient electron transport and blocks holes, thereby reducing recombination losses.
- Buffer Layer: Cadmium Sulfide (CdS) is used as the buffer layer. It provides an excellent interface with the CFTS absorber, facilitating efficient charge separation and transport. The thickness of the CdS layer is set at 200 nm [13].
- HTL layer: NiO_x, Cu₂O, and CuI are taken as HTL layers, to get replaced and effective hole transport from the absorber layer to the back contact, because of their excellent stability, appropriate valence band alignment with the CFTS absorber, and high hole mobility.
- Absorber Layer: The primary absorber layer is CFTS (Copper Iron Tin Sulfide), with a thickness of 400 nm [13]. This layer is responsible for absorbing photons and generating electron-hole pairs.
- Top Contact: Aluminum (Al) is used as the top contact due to its good electrical conductivity and ability to form a low-resistance contact with the HTL.

Table 4

The properties of back and front contacts [71,72].

Parameters	ITO	Al
Metalwork function (eV)	4.7	4.2
SRV of electron (cm ⁻²)	10 ⁵	10 ⁷
SRV of holes (cm ⁻²)	10 ⁷	10 ⁵

3. Simulation methodology

The global air mass 1.5 (AM 1.5G) reference spectrum with an irradiance of 1000 W/m² is considered the light source for the solar cell simulations. The device is illuminated through the ITO contact, and all performance evaluations are conducted at room temperature. The drain-in efficiency of kesterite models like CFTS is influenced by the presence of bulk and interface traps, which arise from defects such as antisite and vacancy defects [73–76]. These defects lead to various recombination mechanisms, including Shockley-Read-Hall (SRH), radiative, non-radiative and Auger recombinations [23,75,77,78]. The bulk defect density for CFTS is set at 1×10¹⁶ cm⁻³, with donor-type characteristics and uniform energy distribution across all simulations [72]. CFTS thin films prepared via sputtering or solution-based methods typically exhibit low carrier lifetimes and carrier concentrations in the range of 1 × 10¹⁴ to 1 × 10¹⁷ cm⁻³. These lifetimes are consistent with defect densities between 1 × 10¹⁵ and 1 × 10¹⁷ cm⁻³, varying according to synthesis and post-treatment conditions. Similarly, defect characterization methods such as Deep Level Transient Spectroscopy (DLTS) identify antisite defects and vacancies in kesterite compounds with defect densities within the same range [50,79]. The occurrence of Cu–Fe antisite disorder is supported by the minimal difference in ionic radii, making a mid-gap defect density of ~1 × 10¹⁶ cm⁻³ plausible. Notably, simulations incorporating bulk defect densities between 1 × 10¹⁵ and 1 × 10¹⁷ cm⁻³ showed minimal impact on overall device performance. Increasing the bulk defect density in our subsequent calculations shows similar results with the same efficiency values.

To thoroughly investigate practical scenarios during the fabrication of CFTS solar cells, interface defect concentrations at the HTL/CFTS, CFTS/CdS, and CdS/TCO interfaces are also taken into consideration, as given in [Table 5](#).

Initially, the influence of hole transport layer (HTL) thickness on device performance was examined by varying it from 10 nm to 100 nm. Based on the optimized thickness for each HTL, the corresponding device behavior was investigated by analyzing the electric field distribution, carrier generation rate, and recombination rates. Keeping the HTL thickness constant at its optimized value, the shallow acceptor density in all HTLs was varied from 1 × 10¹⁴ to 1 × 10²⁰ cm⁻³ to study its impact on device performance and the associated changes in electric field, generation rate, and recombination rate. Subsequently, interface defect density was varied between 1 × 10¹⁰ and 1 × 10¹⁵ cm⁻², incorporating

Table 3

The layer properties used as input for the CFTS solar cell simulations.

Parameters	CFTS [19–23]	NiO _x [65]	Cu ₂ O [65]	CuI [66]	ZnO [67]	CdS [68]
Thickness (μm)	1	(0.01–0.1)	(0.01–0.1)	(0.01–0.1)	0.1	0.2
Band gap (eV)	1.5	3.8	2.17	3.1	3.4	2.4
Electron affinity	3.98	1.4	3.2	2.1	4.55	4.5
Dielectric permittivity (eV)	6.6	10.7	7.11	6.5	9	9
CB effective density of states (cm ⁻³)	2.2x10 ¹⁸	2.0x10 ¹⁹	2.02x10 ¹⁷	2.8x10 ¹⁹	4x10 ¹⁸	2.2x10 ¹⁸
VB effective density of states (cm ⁻³)	1.8x10 ¹⁹	1.8x10 ¹⁹	1.1x10 ¹⁹	1x10 ¹⁹	9x10 ¹⁹	1.8x10 ¹⁹
Electron thermal velocity (cm/s)	1x10 ⁷					
Hole thermal velocity (cm/s)						
Electron mobility (cm ² /v.s)	25	12	20	20	50	100
Hole mobility (cm ² /v.s)	21.98	28	80	43.9	20	25
Shallow uniform donor density (cm ⁻³)	0				5x10 ²⁰	1x10 ¹⁸
Shallow uniform acceptor density (cm ⁻³)	3x10 ¹⁸	1x10 ²⁰	1x10 ¹⁸	1x10 ¹⁸	10	0
Work function/VBM-CBM (eV)	-5.5, -3.98 [26]	-5.4, -1.8 [26]	-5.4, -3.2 [26]	-5.4, -2.8 [16]	-7.52, -4.26 [69]	-6.92, -4.5 [70]

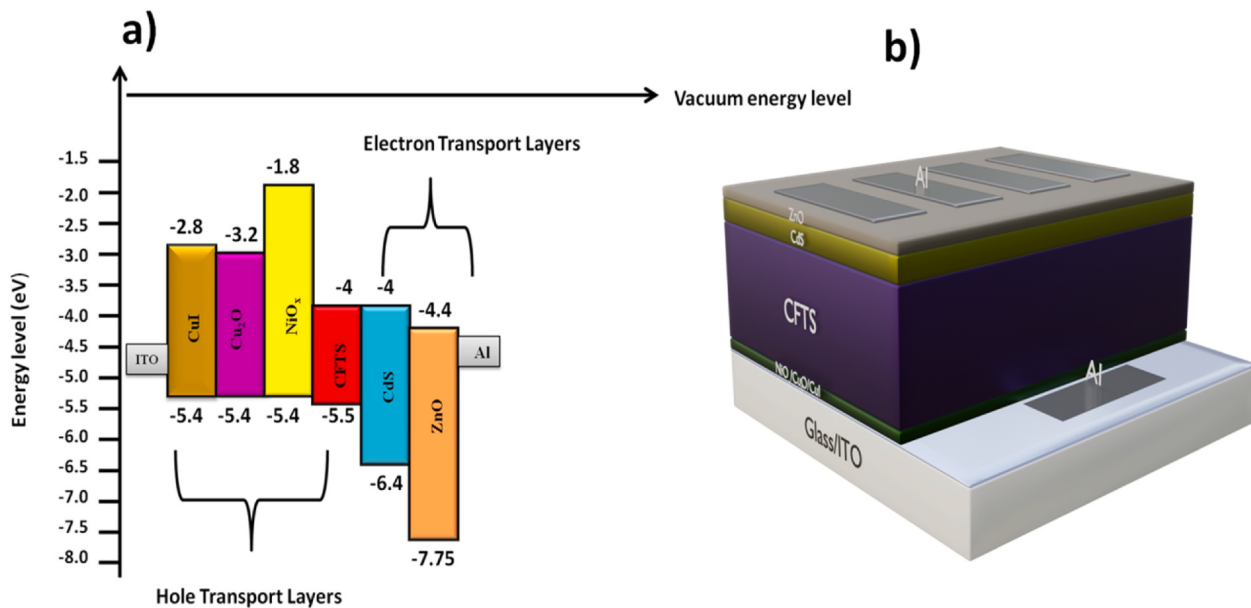


Fig. 2. a) Energy band diagram of the different layers used in the simulation of CFTS solar cells,b)Proposed CFTS device structure.

Table 5

The defect density levels used in the device simulations [72].

Device parameter	Defect density (1/cm ³)
CFTS absorber (bulk)	1x10 ¹⁶
CFTS/NiO _x interface (Surface)	1x10 ¹⁰
CFTS/Cu ₂ O interface	
CFTS/CuI interface	
CFTS/CdS interface	1x10 ¹⁰ -1x10 ¹⁵
CdS/ZnO interface	—
Device parameter	Defect density (1/cm ³)

the previously optimized thickness and acceptor densities, and its effect on the same device parameters was evaluated.

Finally, after determining the appropriate interface defect density, the influence of series resistance (ranging from 1 Ω cm² to 10 Ω cm²) and shunt resistance (from 100 Ω cm² to 1000 Ω cm²) on device performance was systematically analyzed.

4. Results and discussion

4.1. Impact of various hole transport layers (HTLs)

4.1.1. Effect of layer thickness

Optimizing the thickness of the hole transport layer is critical because it has a significant impact on the performance of the CFTS solar cell. If the HTL is extremely thin, it will not cover the active region and might not provide enough barrier for the hole injection, which will cause the charge extraction to be incomplete and recombination to increase. Increased series resistance and difficulty in extracting charges are caused by hole transport, which lowers efficiency and causes energy loss when the HTL thickness is too high. The energy band diagram of the simulated device is shown in Fig. 3. To minimize recombination at the interface between the HTL layers, optimized thickness ensures effective charge separation and transport of holes. The proposed device structure is ITO/HTL/CFTS/CdS/ZnO/Al, with ZnO acting as the transparent conducting layer (TCO), and the thickness of the hole transport layer (HTL) NiO_x, Cu₂O, and CuI was varied from 10 nm to 100 nm while keeping the thickness of ZnO constant at 10 nm as the ETL. It was found that the device's performance remained largely unaffected by the thickness of the NiO_x as the HTL layer Fig. 4a. Conversely, with Cu₂O, an

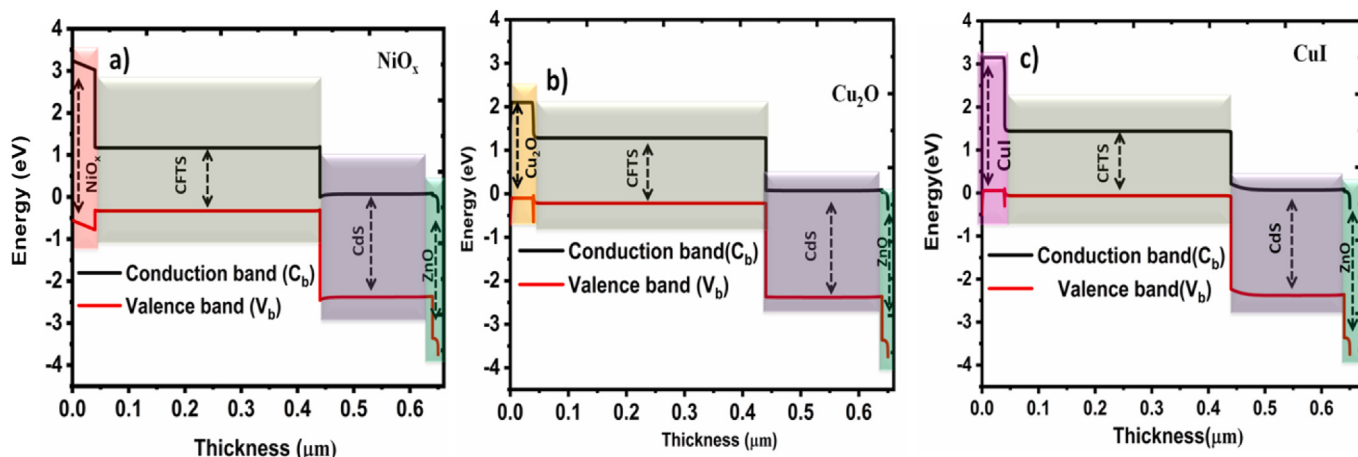


Fig. 3. Energy band diagram of the layers from the SCAPS-1D simulation software.

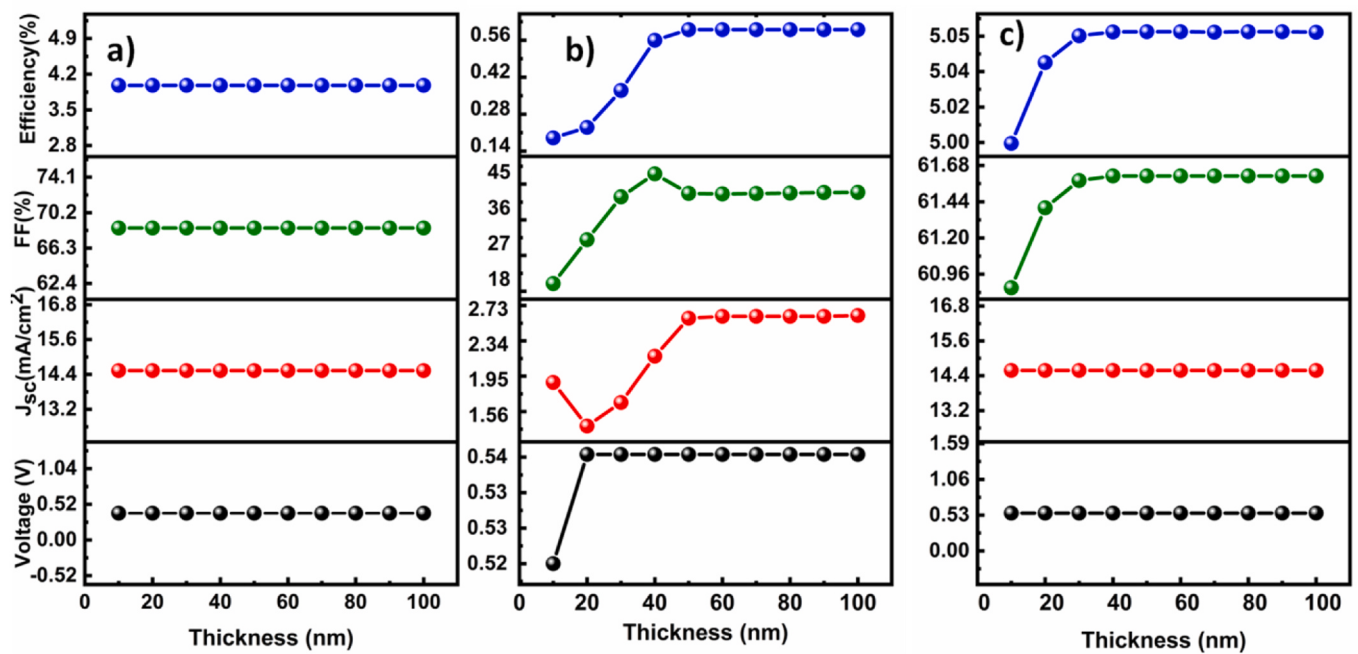


Fig. 4. Effect of thickness of HTL on the performance of solar cell characteristics (a) NiO_x (b) Cu_2O (c) CuI .

increase in thickness resulted in a noticeable enhancement in efficiency, achieving a relatively low efficiency ranging from 0.19 % to 0.61 % with V_{oc} at 0.54 V Fig. 4b. Increasing the thickness of Cu_2O reduces its conductivity [80], leading to higher ohmic losses that distort the I-V characteristics and lower the fill factor (FF). As the Cu_2O layer thickens, the built-in electric field at the absorber interface weakens, making it more likely for photogenerated carriers to recombine before being collected. This degrades junction quality and causes deviations from ideal diode behavior, further reducing the FF. Beyond 50 nm, Cu_2O becomes counterproductive due to its inherent resistivity, low hole mobility, and a recombination-prone interface all of which contribute to a significant potential drop and decreased FF. The short circuit current density remained consistent at 2.6 mA/cm^2 after a thickness of 50 nm, while a notable rise in fill factor was observed from 19.92 % at 10 nm to 47.59 % at 50 nm, subsequently declining to 42.95 % at higher thicknesses.

This can be attributed to voltage drops induced by traps within the bulk and CFTS/CdS interfaces [20,21]. In contrast, an increase in HTL thickness with CuI exhibited significant improvement in device performance, achieving a maximum efficiency of 5.05 % with V_{oc} at 0.56 V, current density at 14.57 mA/cm^2 , and fill factor at 61.61 % at a thickness of 50 nm as in Fig. 4c, representing the optimal thickness for peak CFTS solar cell efficiency. Further increases in the hole transport layer thickness beyond 50 nm might lead to self-absorption, hindering light penetration to the absorber layer and consequently diminishing overall device performance. Further, to understand the device performance and to optimize the suitable thickness in detail, it is very important to understand the electric field, generation rate, and recombination rate, at three different thicknesses 10 nm, 50 nm, and 100 nm which is reflected in J-V characteristics Fig. S1 and quantum efficiencies Fig. S2 (Supporting information). The impact of these factors on devices with varying thicknesses (10 nm, 50 nm, and 100 nm) was examined.

The electric field is crucial for analyzing mechanisms within solar cells; a strong electric field enhances charge separation and increases the short-circuit current, while a weak electric field results in higher recombination rates, reducing the short-circuit current and overall efficiency. Fig. 5 illustrates the effect of the electric field on three different HTLs. NiO_x has a relatively high VBM and CBM, as in Table 3, creating a strong built-in potential at the HTL/CFTS interface, enhancing the

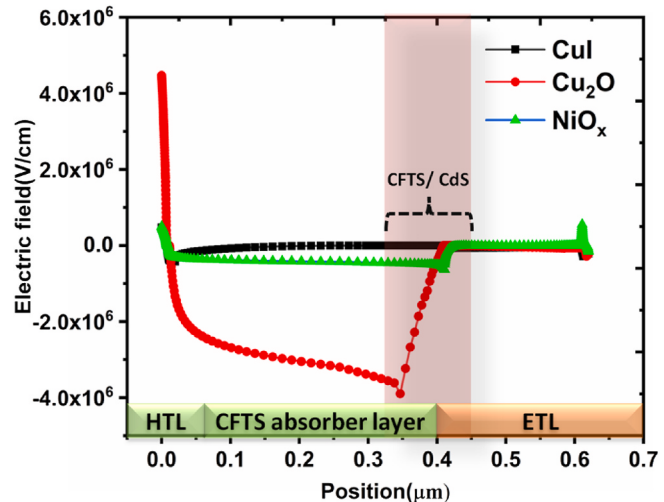


Fig. 5. Electric field for NiO_x , Cu_2O , and CuI layer thicknesses of 50 nm.

electric field. The electric field distribution at the ITO/HTL interfaces was found to be significantly impacted by varying NiO_x thickness which could be attributed to variations in energy levels or work functions, which in turn prompt band bending and charge separation. Whereas Cu_2O has a moderate VBM and CBM value, leading to an optimal electric field at the $\text{Cu}_2\text{O}/\text{CFTS}$ interface, less than that of NiO_x . At 10 nm, the Cu_2O layer is thin enough to create a strong built-in potential across the CFTS/CdS interface, and the electric field direction aids in efficient carrier separation, with the field driving electrons toward the CdS layer and holes toward the CFTS layer. The potential drop within the thicker Cu_2O layer (50 nm) might cause a reversal of the electric field polarity at the CFTS/CdS interface. This reversal can result in an unfavorable electric field that drives electrons and holes in opposite directions, possibly increasing recombination and reducing device performance [1]. The additional thickness of 100 nm can cause the electric field to redistribute once again, potentially reversing back to the original polarity. This is due to the combined effects of the potential drops across all

layers and the need to maintain charge neutrality and continuity of the electric field across the interfaces. The efficiency of charge extraction depends on the field at the interface, hole mobility, rate of hole transfer, and the energy at the interface, which will be reduced at low thickness [81]. The less favorable increase in the electric field with NiO_x compared to Cu_2O and CuI could be attributed to NiO 's higher work function leading to less favorable band alignment, higher defect density at interfaces, potentially lower interface quality, and lower hole mobility. These factors contribute to a weaker built-in potential and electric field at the CFTS/CdS interface, reducing the efficiency of charge carrier separation and overall device performance. The total generation rate for the devices using HTL was analyzed at thicknesses of 10 nm, 50 nm, and 100 nm. Depletion regions formed at CFTS/CdS and CdS/ZnO junctions contribute to increased carrier generation. The electric field in the depletion region helps to quickly separate photo-generated electron-hole pairs, improving the overall generation rate. The transfer of electrons from CdS to ZnO results in the formation of an electric field across the interface. This field opposes further electron flow and establishes a built-in potential and a corresponding negative charge builds up in the depletion region of ZnO.

As the electric field reflects in the charge generation and the separation at the interfaces, it is necessary to understand the rate of charge generation at different thicknesses Fig. S8 (Supporting information). The HTL layer affects charge carrier generation in the bulk CFTS and CdS layers indirectly by influencing the electric field distribution and interface defect density. A well-optimized HTL enhances the electric field, passivates interface defects, maintains transparency, and minimizes series resistance, all of which contribute to efficient charge generation, separation, and collection. Conversely, a poorly optimized HTL can lead to unfavorable electric fields, increased recombination, reduced light absorption, and higher series resistance, all of which negatively impact carrier generation and overall device performance.

4.1.1.1. Electric field, generation rate, recombination rate. Charge carrier concentration was measured at the CFTS/CdS interfaces for devices using NiO_x , Cu_2O , and CuI as hole transport layers (HTLs), as in Fig. 6. The generation rates increased with the addition of an HTL, which promoted excess holes to the layers, enhancing carrier density and efficiency while reducing recombination possibilities.

When the generation rate is high, the HTL thickness must be optimized to effectively accommodate charge carriers. Charge carrier concentration was measured at the CFTS/CdS interfaces for devices using NiO_x , Cu_2O , and CuI as hole transport layers (HTLs). In contrast to Cu_2O

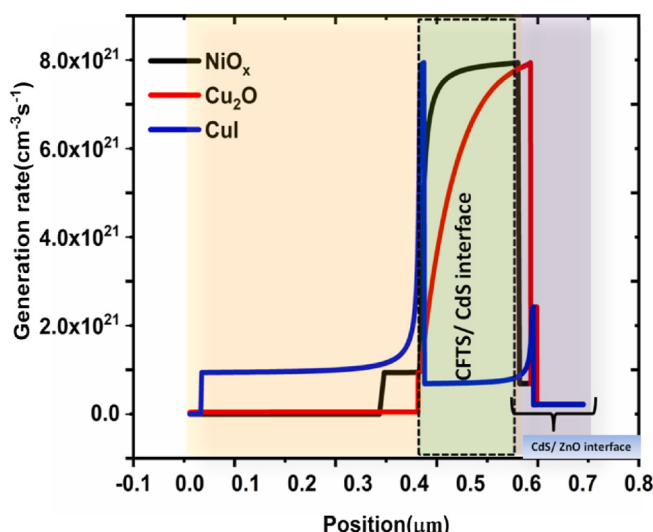


Fig. 6. Generation rate for HTL layer thicknesses of 50 nm for the layers NiO_x , Cu_2O , and CuI .

and NiO_x , a sharp rise in the generation rate of $8 \times 10^{21} \text{ cm}^{-3}\text{s}^{-1}$ is shown in the case of CuI at 400 and 600 nm. This is because there is less recombination, which leads to good band alignment and an enhanced electric field.

However, significant differences in charge generation were noted in Cu_2O at 50 nm and 100 nm, indicating that 50 nm is the optimal thickness for maximum efficiency. When the generation rate is high, the HTL thickness must be optimized to effectively accommodate charge carriers.

The influence of the recombination rate can detail the mechanism that may occur at device interfaces, similar to the generation rate. Cu_2O and CuI displayed increased recombination at the interfaces as in Fig. S8 (supporting information), but thickness had no significant influence on recombination for NiO_x . Recombination rates indicate the cause of the efficiency drain and the rate of recombination is higher for each hole transport layer, with NiO_x expressing at the ITO/ NiO_x interface, Cu_2O exhibiting at the ITO/ Cu_2O , CFTS/CdS, ZnO/Al, and CuI showing at the ITO/ CuI and CFTS/CdS interfaces. Recombination rates increased beyond the optimal thickness range of 50 nm, reaching higher levels at 100 nm. The influence of thickness is also reflected in the J-V characteristics and quantum efficiency of the devices, as shown in the supporting information (Figs. S1 and S2). Summarizing all intrinsic factors such as electric field, generation rate, and recombination rate, the optimal HTL thickness is determined to be 50 nm.

4.1.2. Effect of shallow acceptor densities

Shallow acceptors are those that bring in energy levels that are near to the semiconductor's valence band, take electrons from the band, and leave behind holes that increase the concentration of holes in the material, making it more p-type. The shallow acceptor density within the hole transport layer (HTL) was varied from 1×10^{14} to $1 \times 10^{20} \text{ cm}^{-3}$ while keeping the HTL thickness constant at 50 nm. Observations revealed that altering the acceptor density in the HTL affected the solar cell performance of CFTS, leading to variations in efficiency. Notably, while the open-circuit voltage (V_{oc}) and short-circuit current density (J_{sc}) remained unchanged; differences were observed in the fill factor and overall efficiency. These changes are likely due to improved interface performance, which reduces recombination losses during charge carrier transport.

As the doping concentration increases, charge separation will improve, enhancing efficiency. Higher doping concentrations increased the electric field within the device, improving charge separation and enabling more effective movement of carriers to their respective n and p regions. This also increased charge carrier mobility, allowing carriers to move more quickly to the contacts, thereby reducing recombination possibilities and improving solar cell performance. Specifically, the open-circuit voltage remained stable at 0.4 V, while the current density increased from 14.03 mA/cm^2 to 14.51 mA/cm^2 . A significant increase in the fill factor was observed, ranging from 26.22 % to 68.51 %, leading to an efficiency rise from 1.47 % to 3.98 %. At higher doping levels, hole mobility surpassed the effects of ionized impurity scattering, whereas at lower acceptor densities, internal lattice scattering dominated over hole mobility [82,83]. Increased acceptor density positively influenced hole mobility, enhancing charge separation, conductivity, and overall device performance. However, excessive doping ($>10^{20} \text{ cm}^{-3}$) could lead to the formation of Coulomb traps, which adversely affected the device's performance, highlighting the importance of optimizing the acceptor density [84]. Higher values of acceptor densities inherently don't create the columb trap, instead, it will undergo self-compensation. Excess acceptors like Cu vacancies and Cu interstitials are counterbalanced by donor-type point defects, which will mitigate the net free carriers and introduce Coulomb scattering centers [85]. Copper interstitials act as donor-like defects, which will limit the achievable hole concentration due to charge neutrality constraints and Fermi level pinning [85–87]. Similarly, ionized acceptors and donors will create potential fluctuation and act as coulomb scattering [88].

The impact of shallow acceptor density on CFTS solar cell performance is illustrated in Fig. 7. By varying the shallow acceptor density while incorporating Cu₂O, noticeable enhancements in solar cell parameters were observed, underscoring the influence of acceptor density while holding all other parameters constant. Interestingly, V_{oc} showed minimal variation, ranging from 0.5 to 0.51 V for acceptor densities between 1×10¹⁴ and 1×10¹⁷ cm⁻³, with a subsequent increase beyond this optimal range. Similarly, the current density increased from 0.23 mA/cm² to 0.33 mA/cm² within the optimal region before a sudden deviation in device performance was observed. Upon reaching a doping concentration of 1×10¹⁷ cm⁻³, there was a notable increase in fill factor from 27.9 % to 41.9 % and inefficiency from 0.04 % to 3.32 % as in Fig. 7b. Additionally, an increase in the acceptor density of CuI resulted in an efficiency enhancement from 4.4 % to 5 %. The open-circuit voltage (V_{oc}) remained stable at 0.56 V with insignificant changes, while the current density initially increased from 14.54 mA/cm² to 14.57 mA/cm² before slightly declining to 14.54 mA/cm² shown in Fig. 7c. Notably, there was a substantial increase in fill factor from 53.9 % to 61.8 %, indicating higher maximum power generation with increased acceptor density in this device structure.

The effects of the electric field, generation rate, and recombination rate of the device were analyzed for acceptor densities of 1×10¹⁴, 1×10¹⁸, and 1×10²⁰ cm⁻³. With 50 nm HTL thickness, the impact of different acceptor densities is shown in Fig. 8. A significant electric field was observed in CuI, particularly in the 0.1 μm–0.4 μm range as the acceptor density increased. A drastic change was noted at an acceptor density of 1×10²⁰ cm⁻³, indicating the presence of an intrinsic electric field in the device. A slight increase in the electric field was observed for the HTL Cu₂O at an acceptor density of 1×10¹⁹ cm⁻³, with further increases at higher densities. The increased electric field at optimal or higher acceptor densities enhanced the separation and extraction of photo-generated carriers, resulting in higher photocurrents and power conversion efficiencies. The electric field is wider at the CFTS/CdS interfaces increasing the acceptor densities, which may be due to the increased build-in potential.

When increasing the shallow acceptor density of the hole transport layer to 1×10¹⁴, 1×10¹⁸, and 1×10²⁰ for NiO_x, Cu₂O, and CuI, it is observed that the highest charge carrier generation occurs at the CFTS/CdS interface with an acceptor density of 1×10²⁰ cm⁻³. Among these, CuI

yields the highest charge carrier generation, followed by Cu₂O and NiO_x. A comparison of the generation rate for three acceptor densities 1×10¹⁴, 1×10¹⁸, and 1×10²⁰ for the three-hole transport layers NiO_x, Cu₂O, and CuI shows remarkable change in Fig. S10 (supporting information). The optimal charge carrier separation and generation are noted between acceptor densities of 1×10¹⁸ and 1×10²⁰. This enhancement is likely attributed to the built-in potential created by the electric field at the interface, which effectively drives charge carriers through the metal contacts. The higher mobility of electrons and holes in the case of Cu₂O and CuI may be the reason for the generation rate especially at higher acceptor densities.

Conversely, the recombination rate also increased at higher acceptor densities, particularly at the CFTS/CdS interfaces, as shown in Fig. 9. At these higher densities, the recombination rate was lower at the CuI/CFTS interface but higher at the CFTS/CdS interface. A sudden decrease in fill factor at an acceptor density of 1×10¹⁹ cm⁻³ in Cu₂O, shown in Fig. 7b, may be due to increased recombination loss at the interfaces. Recombination rates will increase with shallow acceptor density, leading to a rise in non-radiative recombination and the potential generation of oxygen vacancies. This will also cause self-compensation, neutralizing the acceptor states and creating donor vacancies, thereby decreasing mobility. The saturation of short-circuit current, observed (supporting information), which may be due to limits in light absorption and charge separation, with a decrease caused by increased recombination at the CFTS/CdS interfaces.

4.1.3. Effect of CFTS/CdS interface defect density

The concentration of defects or trap states between the several layers of solar cells is referred to as interface defects which play a vital role in the performance of solar cells. Interface defect states refer to electrically active imperfections per unit area at the heterojunction. In this case, the CFTS/CdS interface, expressed in cm⁻². In this work, we consider a range of interface defect densities from an ideal value of 1 × 10¹⁰ cm⁻² to a poor interface at 1 × 10¹⁵ cm⁻². These defects serve as recombination centers for charge carriers, leading to losses in open-circuit voltage (V_{oc}), short-circuit current density (J_{sc}), fill factor (FF), and overall device efficiency (η) [50,79,88]. Cu_{Fe} antisites are formed due to their similar ionic radii, copper and iron can readily exchange lattice positions, particularly under varying temperature conditions. This

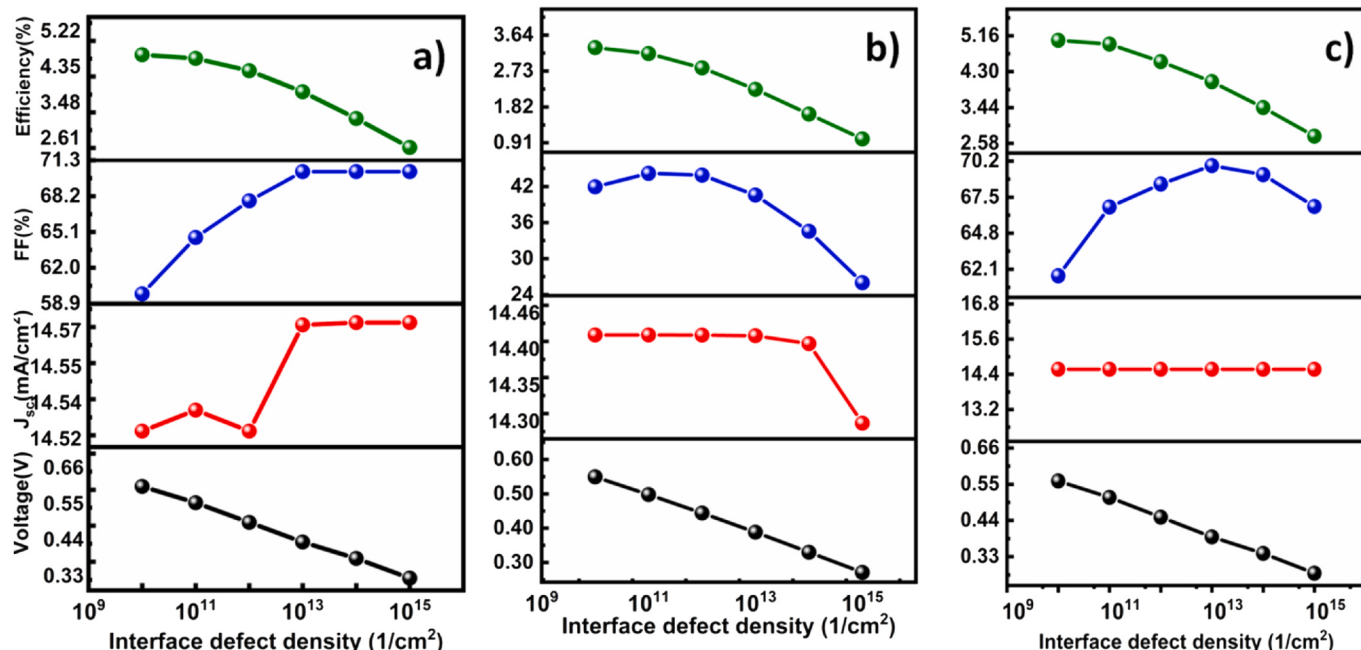


Fig. 7. The effect of shallow acceptor density of HTL, a) NiO_x, b) Cu₂O, and c) CuI, on the performance of solar cells.

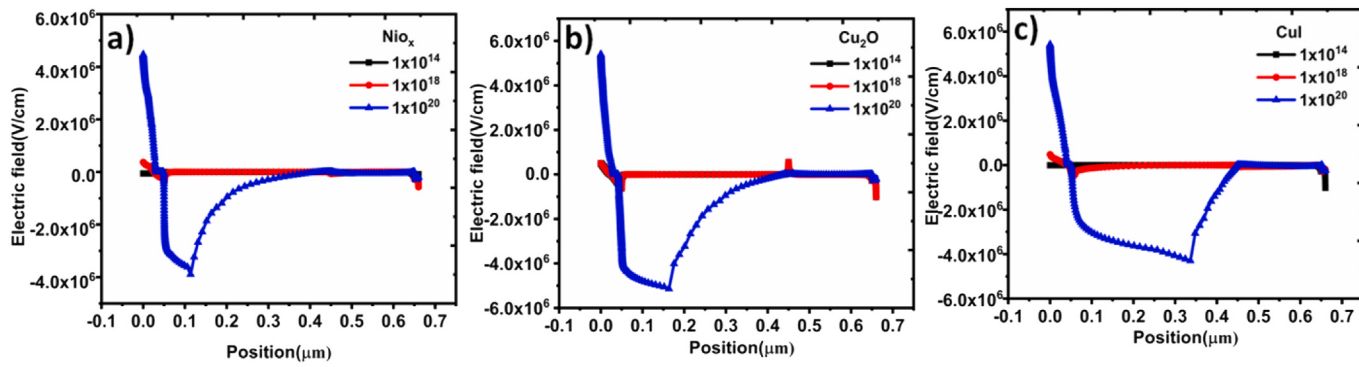


Fig. 8. Electric field for HTL at acceptor densities of 1×10^{14} , 1×10^{18} , and $1 \times 10^{20} \text{ cm}^{-3}$ in (a) NiO_x , (b) Cu_2O , and (c) CuI .

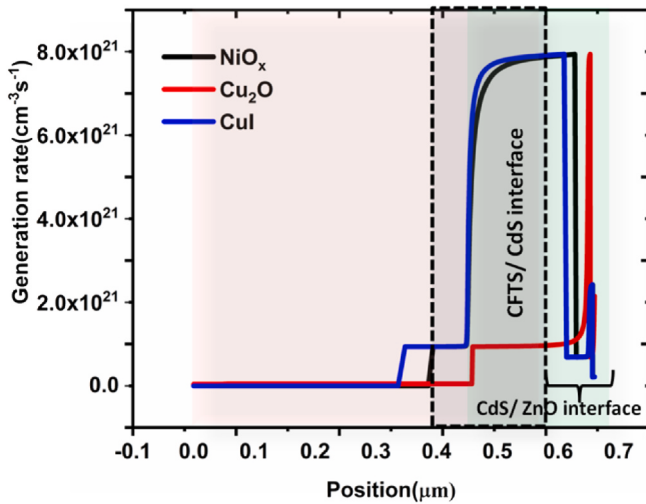


Fig. 9. Generation rate for HTL at acceptor densities of $1 \times 10^{20} \text{ cm}^{-3}$ in NiO_x , Cu_2O , and CuI .

cation disorder leads to the formation of deep donor-like defects near the mid-gap, which significantly enhances non-radiative recombination [42, 73, 85]. Additionally, improper bonding at the interface results in the formation of interface trap states. In the case of Sulfur vacancy, especially during high-temperature deposition, sulfur vacancies are likely to form, particularly at the CFTS surface and at the interface with CdS . These vacancies can behave as donor-like defects, often introducing deep-level states, especially when coordinated with Fe and Sn atoms. Such defects can create mid-gap trap states, typically modeled within the range of 1×10^{13} to $1 \times 10^{15} \text{ cm}^{-2}$. Fe_{Cu} are formed due to the similar ionic radii of Fe and Cu, Fe can substitute at Cu sites, introducing relatively shallow acceptor levels that may contribute to band tailing.

Here interface defect density was varied from 1×10^{10} to $1 \times 10^{15} \text{ cm}^{-2}$, and the results are shown in Fig. 10. For NiO_x , the optimal interface defect density for device performance was found to be $1 \times 10^{13} \text{ cm}^{-2}$, as supported by experimental validation from the literature [13]. For other HTLs, the minimum interface defect density was set at $1 \times 10^{10} \text{ cm}^{-2}$, which represents the lowest achievable defect density for these layers [36]. Increasing the interface defect density raises the likelihood of recombination centers forming, leading to higher probabilities of photo-generated carriers recombining at the interfaces. The presence of trap centers within the interfaces reduces the efficiency of CFTS solar cells, as these traps diminish the overall device performance. Trap sites,

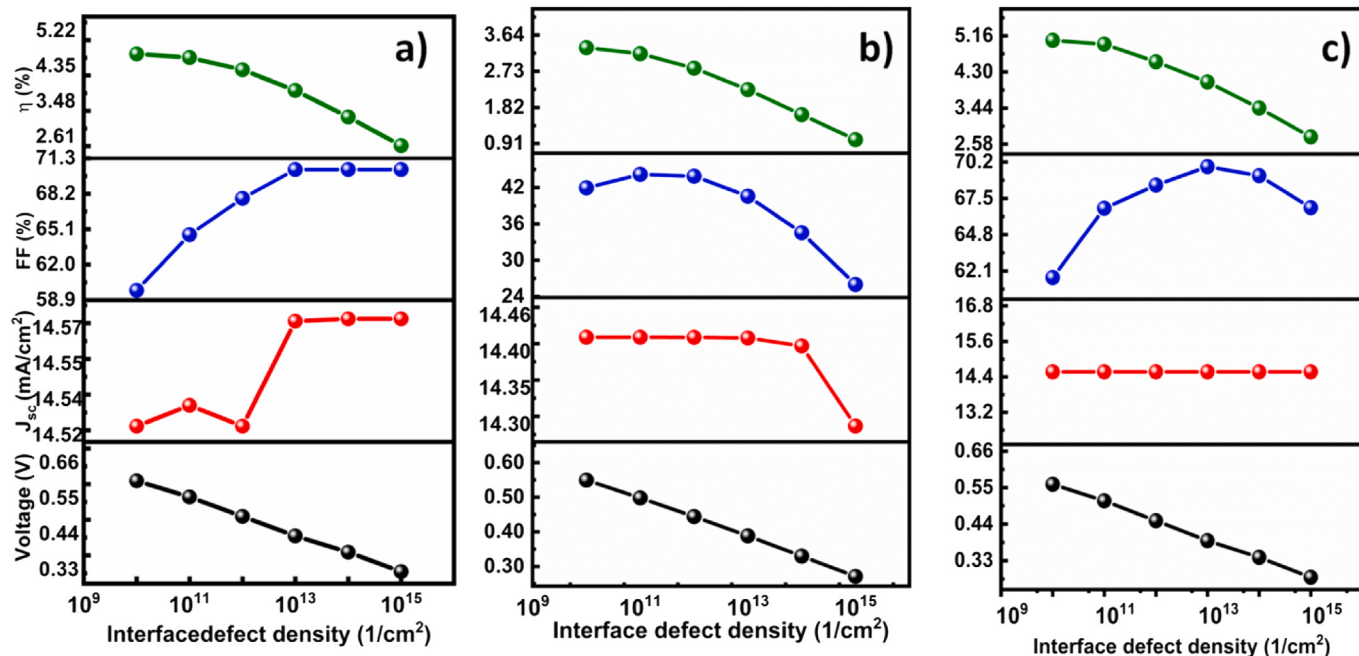


Fig. 10. Solar cell characteristics with interface defect densities varied from 1×10^{10} to $1 \times 10^{15} \text{ cm}^{-2}$ for a) NiO_x b) Cu_2O and c) CuI hole transport layers.

often due to antisite defects, can act as donors, acceptors, or neutral centers [22,73]. In this study, neutral defects at the NiO_x/CFTS and CFTS/CdS interfaces were considered. The p-n interface has a greater influence than p-p interfaces due to p-n recombination, which increases carrier recombination and decreases solar cell efficiency. Similar effects were observed for CuI and Cu_2O . For an interface defect density of $1 \times 10^{15} \text{ cm}^{-2}$, CuI achieved an efficiency of 2.81 % with V_{oc} of 0.283 V, a current density of 14.54 mA/cm^2 , and a fill factor of 68.43 %. In contrast, Cu_2O at this defect density showed an efficiency of 1 % with V_{oc} of 0.271 V, a current density of 14.28 mA/cm^2 , and a fill factor of 64.43 % shown in Fig. 10c. This variation highlights differences in device performance among the three HTLs. For CuI , interface defect densities did not significantly affect the electric field, generation rate, or recombination rate. However, for devices using Cu_2O and NiO_x as HTLs, increased defect densities led to a decrease in fill factor.

CuI maintained a strong electric field across all interface defect densities, which could be attributed to changes in short-circuit current. Similar effects were noted for NiO_x and Cu_2O as in Fig. S7 (supporting information). Notably, at an interface defect density of $1 \times 10^{13} \text{ cm}^{-2}$, Cu_2O showed the highest defect density and an increased generation rate shown in Fig. 11. The observed decrease in fill factor for NiO_x and CuI likely results from increased recombination losses, which is also, reflected in the efficiencies of the CFTS solar cells. There was no change in generation rate in the case of CuI as a hole transport layer, whereas for NiO_x and Cu_2O at the interface defect densities $1 \times 10^{13} \text{ cm}^{-2}$ and $1 \times 10^{15} \text{ cm}^{-2}$, maximum charge generation happens at $0.1\text{--}0.4 \mu\text{m}$ on increasing the interface defect density. This means that the maximum charge generation happens at the bulk in the case of NiO_x and Cu_2O with an interface defect density of $1 \times 10^{13} \text{ cm}^{-2}$ as in Fig. 11. Electric field and recombination study for three different interface defects were analyzed for all HTLs as shown in Figure S6 and Figure S7(supporting information). Interface defects act as recombination centers leading to non-radiative recombination and shorter carrier lifetime. Additionally, in the case of NiO_x and Cu_2O , there is a possibility of forming oxygen vacancies with sub-bandgap levels further lowering the generation rate.

4.2. Impact of series and shunt resistance

In our study, we enhanced the performance of the CFTS solar cell using CuI hole transport layer and ZnO transparent conducting oxide layer. Furthermore, we investigated the effects of series and shunt resistance on the device performance to understand their practical implications. Specifically, we increased the series resistance from $1 \Omega\text{cm}^2$ to $10 \Omega\text{cm}^2$ and simulated its impact on the device characteristics as shown in Table 7. This increase in series resistance led to a reduction in efficiency from 4.9 % to 3.7 %, primarily due to a decrease in the fill factor from 59.8 % to 46.15 %. The open-circuit voltage was slightly dropped from 0.57 V to 0.56 V as the series resistance increased to 2

Table 6

Performance parameters of the solar cell devices without and with the hole transport layer (This work).

Device structure	V_{oc} (V)	J_{sc} (mA/cm^2)	FF (%)	Efficiency (%)
ITO/CFTS/CdS/ZnO/Al	0.282	14.15	69.91	2.79
ITO/CuI (50 nm)/CFTS/ZnO/Al	$0.562 \pm$	$14.55 \pm$	$62.43 \pm$	5.05 ± 0.01
ITO/NiO _x (50 nm)/CFTS/CdS/ZnO/Al	0.00	0.00	0.01	
ITO/Cu ₂ O (50 nm)/CFTS/CdS/ZnO/Al	0.563 \pm	14.511 \pm	59.78 \pm	4.88 \pm 0.00
ITO/Cu ₂ O (50 nm)/CFTS/CdS/ZnO/Al	0.547 \pm	14.40 \pm	42.13 \pm	3.32 \pm 0.68
ITO/CuI (50 nm)/CFTS/ZnO/Al	0.09	0.98	0.46	

Table 7

The variation of solar cell characteristics such as (a) Open circuit voltage (b) Short circuit current (J_{sc}) (c) Fill factor (%) and (d) Efficiency (%) of ITO/CuI/CFTS/CdS/ZnO/Al device with series resistance.

Series resistance (Ωcm^2)	V_{oc} (V)	J_{sc} (mA/cm^2)	FF (%)	Efficiency (%)
1	0.57	14.57	59.8	4.9
2	0.56	14.56	58.1	4.7
3	0.56	14.55	56.4	4.6
4	0.56	14.54	54.9	4.4
5	0.56	14.53	53.3	4.3
6	0.56	14.52	51.8	4.2
7	0.56	14.5	50.2	4.1
8	0.56	14.49	48.8	3.9
9	0.56	14.47	47.4	3.8
10	0.56	14.46	46.1	3.7

Ωcm^2 and remained unaffected thereafter. This voltage drop results in reduced current and output power, thereby decreasing solar cell efficiency.

We also examined the impact of shunt resistance on device performance, particularly at the CFTS/CdS and CdS/ZnO interfaces, while keeping series resistance constant at $10 \Omega\text{cm}^2$. In chalcogenide solar cells, a threshold shunt resistance in between 300 and $1000 \Omega\text{cm}^2$ has been observed, beyond which a significant improvement in performance occurs [72,89]. For CFTS solar cells, the maximum recorded efficiency is 2.9 %, corresponding to a shunt resistance of $539 \Omega\text{cm}^2$. Based on this, the shunt resistance of CFTS solar cells has been varied from $100 \Omega\text{cm}^2$ to $1000 \Omega\text{cm}^2$ to evaluate its impact. Optimizing material properties such as absorber thickness, doping concentration, and bandgap energy can significantly enhance device performance. Additionally, post-annealing treatments help reduce defect formation and improve crystallinity, particularly at the CFTS/CdS interface. The introduction of buffer layers further minimizes recombination losses, thereby increasing shunt resistance and ultimately improving the efficiency of CFTS solar cells. Here, we have varied the shunt resistance from $100 \Omega\text{cm}^2$ to $1000 \Omega\text{cm}^2$

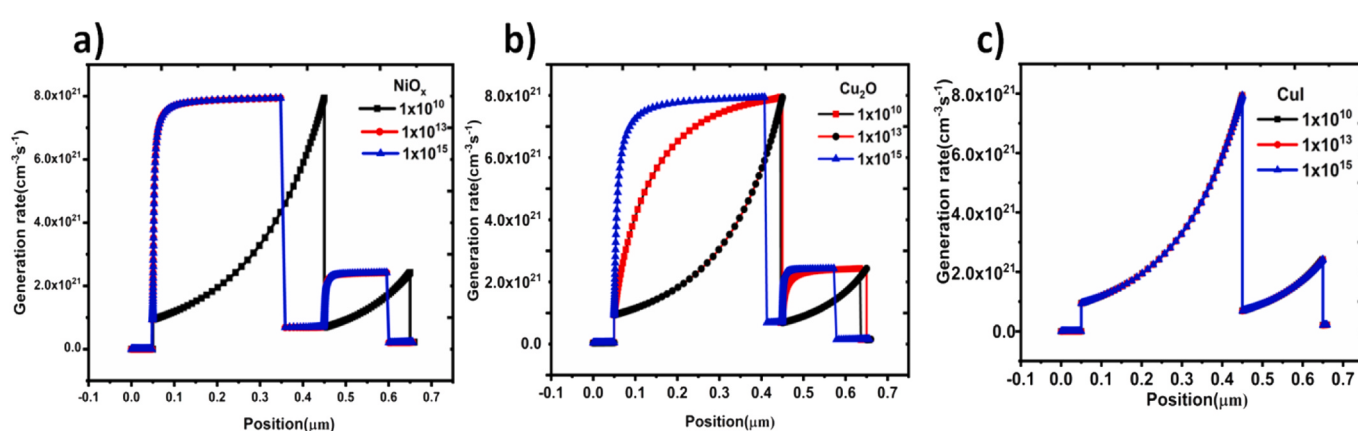


Fig. 11. Generation rate for HTL at interface defect densities of 1×10^{10} , 1×10^{13} , and $1 \times 10^{15} \text{ cm}^{-3}$ in (a) NiO_x , (b) Cu_2O , and (c) CuI .

Ωcm^2 , which yielded a power conversion efficiency of 3.6 %. At 800 Ωcm^2 , the open-circuit voltage (V_{oc}) remained stable, suggesting that this value represents the optimal shunt resistance for achieving maximum output voltage. Shunt resistance significantly affects CFTS solar cell performance by creating unintended current pathways corresponding to imperfections, defects, and grain boundaries within the quaternary material. The presence of maximum possible defects, particularly at the bulk and interfaces, negatively impacts solar cell efficiency. Shunt pathways in the device arise from multiple sources, including the CdS layer, CFTS grain boundaries, secondary phase formation, and irregular layer morphology [41,90]. In particular, a non-uniform CdS layer can leave parts of the underlying CFTS absorber exposed, allowing direct contact with the front electrode and resulting in leakage currents. Pinholes, often caused by suboptimal conditions during chemical bath deposition, especially at low temperatures, can further contribute to this effect [91,92]. The polycrystalline nature of the CFTS layer leads to the formation of grains and grain boundaries, which act as low-resistance channels and are often poorly passivated. These regions may also facilitate the formation of secondary conductive phases and provide diffusion pathways for ions, collectively promoting shunt formation. Link to the fabrication strategies are, Optimal sulfurization facilitates complete sulfur incorporation, thereby eliminating secondary phase formation, promoting grain growth, and minimizing grain boundary density [93] and during CdS deposition, controlling parameters such as pH, deposition time, and precursor concentration ensures uniform coverage with minimal pinholes, while post-deposition annealing helps to densify the CdS layer and eliminate micro-defects [94,95]. The decline in fill factor is attributed to trap states within these regions. Increasing shunt resistance also raised the open-circuit voltage, though this is inconsistent with the expected trend, as shown in Table 8, where leakage current is minimized. Other parameters, such as short-circuit current, fill factor, and efficiency, continue to rise with increasing shunt resistance until they reach a saturation point. We found 800 Ωcm^2 to be the optimum shunt resistance for maximum solar cell performance.

This study examines the device's electrical and structural properties while incorporating the three HTLs NiO_x , Cu_2O , and CuI and attaining a 5.05 % efficiency for the CuI layer. Taking into practical prospects of the device structure ITO/ CuI /CFTS/CdS/ZnO/Al, the band alignment and the lattice match have also been investigated concerning the orientation of the material's planes. The XRD patterns of CFTS and CuI in various studies reveal the preferred growth of their crystallites along (112) and (111) planes when deposited as thin films [96–102]. As seen in Fig. 12, the 3×3 slab model of the Cu_{111} surface has a good lattice match with the 2×2 slab model of the CFTS_{112} surface. This suggests that a better interface can be formed between CFTS and CuI layers during the device fabrication without causing much lattice strain. In terms of lattice compatibility, the CuI/CFTS interface plays a crucial role in determining heterojunction quality. A close lattice match minimizes strain, reduces interfacial dislocations, and suppresses non-radiative recombination. Conversely, lattice mismatch at the CuI/CFTS junction can lead to grain

boundary formation, dangling bonds, vacancy clusters, interstitials, and local strain fields, all of which hinder charge transport and act as recombination centers, thereby reducing device efficiency. Moreover, proper lattice alignment also promotes defect passivation. A well-matched CuI/CFTS interface lowers the formation energy of interface defects and facilitates natural passivation by minimizing dangling bonds and unsaturated coordination sites, further contributing to enhanced device performance. Strain-relieved interfaces can facilitate the migration of copper vacancies in CuI toward adjacent interfacial defect sites. Additionally, iodine or copper interstitials may occupy sulfur or chalcogenide vacancies at the absorber surface. The epitaxial growth of CuI can influence grain orientation in polycrystalline absorbers, thereby reducing grain boundary defect states [37,103]. When CuI is deposited on a sulfur-rich CFTS surface with minimal lattice mismatch, iodide ions may bond with dangling sulfur atoms or stabilize surface states, effectively acting as both a passivation agent and a structural buffer. Overall, improved lattice matching results in fewer interface defects and more effective intrinsic passivation, which collectively enhance carrier lifetime, open-circuit voltage, fill factor, and ultimately device efficiency.

Quantitative strain analysis of HTL/CFTS interface is calculated for CuI , NiO_x and Cu_2O preferably shows (111) plane and the CFTS as (112) plane. The lattice strain was calculated is depicted in Table 9 using the standard mismatch formula. Specifically, the CuI/CFTS interface exhibits a mismatch of around 9.06 %, whereas NiO_x/CFTS and $\text{Cu}_2\text{O}/\text{CFTS}$ show much larger mismatches of 25 % and 23 %, respectively highlighting that CuI/CFTS is far more compatible as.

This can be an additional reason for selecting CuI as the HTL for improved device performance. With these optimized parameters device will be fabricated, which could give approximately 5.05 % efficiency. Also, the impact of appropriate HTL layers on variable acceptor densities with error bars is illustrated in Table 6.

Without HTL, the device exhibits an efficiency of 2.79 %. However, with the incorporation of CuI as the HTL, the efficiency improves significantly to 5.05 %, indicating that CuI is a highly effective HTL material for enhancing the performance of CFTS solar cells. CuI is an intrinsically p-type material attributed to copper vacancies (V_{Cu}). The shallow acceptor density can be effectively optimized by modulating the doping concentration and controlling stoichiometry during deposition. Copper-poor growth conditions promote the formation of additional copper vacancies, thereby enhancing the acceptor density. Furthermore, halide mixing with elements such as Cl^- and Br^- can modify defect formation energies and further increase hole concentration. Employing controlled deposition techniques, such as thermal evaporation, enables precise adjustment of HTL thickness, mitigating CuI degradation. Additionally, low-temperature post-deposition annealing improves interfacial quality by reducing defect states and enhancing film morphology. This study also demonstrates that the performance of photovoltaic devices can be enhanced by incorporating an appropriate hole transport layer (HTL) and minimizing defects in the quaternary chalcogenide material.

5. Conclusion

Using SCAPS 1-D simulation through thorough analysis, this work investigates the realistic efficiency limits of CFTS solar cells with an emphasis on the influence of hole transport layers (HTLs). Our findings shed crucial light on enhancing HTL materials and understanding shunt resistance and series resistance impacts on CFTS device performance. Thickness, shallow acceptor density, and interface defect density of HTLs like NiO_x , Cu_2O , and CuI have a major impact on CFTS solar cell performance. However, with V_{oc} 0.56V and FF 62.4 % CuI , significant performance improvements were demonstrated in varying the thickness, shallow acceptor density, and interface defect densities to reach the efficiency of 5.05 %. HTL influenced in-depth studies of the electric field, generation rate, and recombination rate, the optimal thickness for

Table 8

Solar cell characteristics of the CFTS solar cell for the device structure ITO/ CuI /CFTS/CdS/ZnO by varying the shunt resistance from 100 Ωcm^2 to 1000 Ωcm^2 .

Shunt resistance (Ωcm^2)	V_{oc} (V)	J_{sc} (mA/cm^2)	FF (%)	Efficiency (%)
100	0.5	13.15	39.01	2.69
200	0.54	13.77	42.84	3.2
300	0.54	13.99	44.23	3.38
400	0.55	14.11	44.7	3.47
500	0.55	14.17	44.89	3.52
600	0.55	14.22	45.02	3.56
700	0.55	14.25	45.08	3.59
800	0.56	14.28	45.15	3.61
900	0.56	14.3	45.3	3.62
1000	0.56	14.31	45.41	3.64

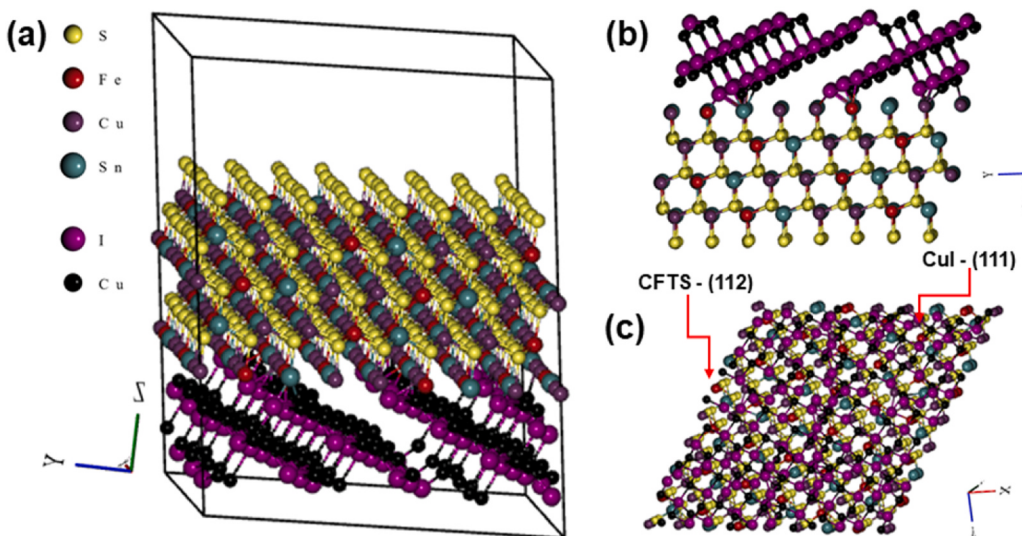


Fig. 12. CFTS/CuI Interface structure.

Table 9
Lattice mismatch of HTL/CFTS Interface.

HTL/CFTS Interface	Lattice parameters of HTL(Å)	Lattice mismatch (%)
CuI/CFTS	$a = b = c = 6.05$ [103]	9.06
NiO _x /CFTS	$a = b = c = 4.17$ [104]	25
Cu ₂ O/CFTS	$a = b = c = 4.27$ [105]	23

maximum efficiency was determined to be 50 nm with interface defect concentrations of $1 \times 10^{10} \text{ cm}^{-2}$ and shallow acceptor densities of $1 \times 10^{18} \text{ cm}^{-3}$. The findings provide useful direction for further research and practical applications, emphasizing the need for precise material and structural changes to achieve optimum solar cell performance. The results highlight the necessity of HTL and structural modifications to attain maximum solar cell efficiency and offer helpful guidance for future research and real-world applications.

CRediT authorship contribution statement

M.K. Jyotsna Raj: Writing – review & editing, Writing – original draft, Validation, Software, Methodology, Investigation, Formal analysis, Conceptualization. **Kallol Mohanta:** Writing – review & editing, Validation, Supervision, Methodology, Investigation, Formal analysis. **Sebin Devasia:** Writing – review & editing, Validation, Supervision, Investigation, Formal analysis. **B. Geetha Priyadarshini:** Writing – review & editing, Validation, Supervision, Methodology, Investigation, Formal analysis, Conceptualization.

Data availability statement

The data that supports the findings of this study are available from the corresponding author upon reasonable request.

Declaration of competing interest

The authors declare that they have no known competing financial interests or personal relationships that could have appeared to influence the work reported in this paper.

Acknowledgments

The authors extend their gratitude to Dr. Marc Burgelman from the Department of Electronics and Information Systems at the University of

Gent in Belgium, for providing the SCAPS-1D simulation software used in this theoretical study. The author also wishes to acknowledge the financial support and facilities provided by the Management of 'PSG & Sons' Charities, Coimbatore, Tamil Nadu, India.

Appendix A. Supplementary data

Supplementary data to this article can be found online at <https://doi.org/10.1016/j.jpcs.2025.113193>.

References

- [1] O.J. Sandberg, J. Kurpiers, M. Stolterfoht, D. Neher, P. Meredith, S. Shoaee, A. Armin, On the question of the need for a Built-in potential in perovskite solar cells, *Adv. Mater. Interfac.* 7 (2020), <https://doi.org/10.1002/admi.202000041>.
- [2] M. Powalla, S. Paetel, E. Ahlswede, R. Wuerz, C.D. Wessendorf, T. Magorian Friedlmeier, Thin-film solar cells exceeding 22% solar cell efficiency: an overview on CdTe-, Cu(In,Ga)Se₂-, and perovskite-based materials, *Appl. Phys. Rev.* 5 (2018), <https://doi.org/10.1063/1.5061809>.
- [3] A. Le Donne, V. Trifiletti, S. Binetti, New earth-abundant thin film solar cells based on chalcogenides, *Front. Chem.* 7 (2019), <https://doi.org/10.3389/fchem.2019.00297>.
- [4] Q. Liu, Z. Cai, D. Han, S. Chen, Natural intermediate band in i 2-II-IV-VI₄ Quaternary chalcogenide semiconductors, *Sci. Rep.* 8 (2018) 2–9, <https://doi.org/10.1038/s41598-018-19935-5>.
- [5] M.S. Kumar, S.P. Madhusudanan, S.K. Batabyal, Substitution of Zn in earth-abundant Cu₂ZnSn(S,Se)4 based thin film solar cells – a status review, *Sol. Energy Mater. Sol. Cells* 185 (2018) 287–299, <https://doi.org/10.1016/j.solmat.2018.05.003>.
- [6] S. Siebenritt, Why are kesterite solar cells not 20% efficient? *Thin Solid Films* 535 (2013) 1–4, <https://doi.org/10.1016/j.tsf.2012.12.089>.
- [7] A.M. Alanazi, F. Alam, A. Salhi, M. Missous, A.G. Thomas, P. O'Brien, D.J. Lewis, A molecular precursor route to quaternary chalcogenide CFTS (Cu₂FeSnS₄) powders as potential solar absorber materials, *RSC Adv.* 9 (2019) 24146–24153, <https://doi.org/10.1039/c9ra02926e>.
- [8] S. Wang, R. Ma, C. Wang, S. Li, H. Wang, Fabrication and photoelectric properties of Cu₂FeSnS₄ (CFTS) and Cu₂FeSn(S,Se)4 (CFTSSe) thin films, *Appl. Surf. Sci.* 422 (2017) 39–45, <https://doi.org/10.1016/j.apsusc.2017.05.244>.
- [9] F. Ghiasi, M.R. Fadavieslam, M. Ardyanian, Facile deposition and study of substrate temperature effect on the structural and physical properties of Cu₂FeSnS₄ (CFTS) thin films, *J. Mater. Sci. Mater. Electron.* 31 (2020) 2398–2405, <https://doi.org/10.1007/s10854-019-02775-y>.
- [10] S.P. Madhusudanan, M. Suresh Kumar, K. Yamini Yasoda, D. Santhanagopalan, S. K. Batabyal, Photo-enhanced supercapacitive behaviour of photoactive Cu₂FeSnS₄ (CFTS) nanoparticles, *J. Mater. Sci. Mater. Electron.* 31 (2020) 752–761, <https://doi.org/10.1007/s10854-019-02582-5>.
- [11] N. Mukurala, S. Suman, A. Bhardwaj, K. Mukurala, S.H. Jin, A.K. Kushwaha, Cu₂FeSnS₄ decorated Ni-TiO₂ nanorods heterostructured photoanode for enhancing water splitting performance, *Appl. Surf. Sci.* 551 (2021), <https://doi.org/10.1016/j.apsusc.2021.149377>.
- [12] R.R. Prabhakar, N. Huu Loc, M.H. Kumar, P.P. Boix, S. Juan, R.A. John, S. K. Batabyal, L.H. Wong, Facile water-based spray pyrolysis of earth-abundant Cu₂FeSnS₄ thin films as an efficient counter electrode in dye-sensitized solar

- cells, *ACS Appl. Mater. Interfaces* 6 (2014) 17661–17667, <https://doi.org/10.1021/am503888v>.
- [13] S. Chatterjee, A.J. Pal, A solution approach to p-type Cu₂FeSnS₄ thin-films and pn-junction solar cells: role of electron selective materials on their performance, *Sol. Energy Mater. Sol. Cells* 160 (2017) 233–240, <https://doi.org/10.1016/j.solmat.2016.10.037>.
- [14] C. Dong, W. Meng, J. Qi, M. Wang, Cu₂FeSnS₄ nanocrystals as effective electron acceptors for hybrid solar cells, *Mater. Lett.* 189 (2017) 104–106, <https://doi.org/10.1016/j.matlet.2016.11.090>.
- [15] C. Dong, G.Y. Ashebir, J. Qi, J. Chen, Z. Wan, W. Chen, M. Wang, Solution-processed Cu₂FeSnS₄ thin films for photovoltaic application, *Mater. Lett.* 214 (2018) 287–289, <https://doi.org/10.1016/j.matlet.2017.12.032>.
- [16] S.P. Madhusudanan, K. Mohanta, S.K. Batabyal, Electrical bistability and memory switching phenomenon in Cu₂FeSnS₄ thin films: role of p-n junction, *J. Solid State Electrochem.* 23 (2019) 1307–1314, <https://doi.org/10.1007/s10008-019-04213-9>.
- [17] S. Kalambur, R. Mouli, N.J. Choudhari, D.M. Kavya, Y. Raviprakash, Exploring the potential of Cu₂FeSnS₄: a comprehensive review on structural properties, optoelectronic features, and future prospects in earth-abundant thin film solar cells, *Cogent Eng.* 11 (2024), <https://doi.org/10.1080/23311916.2024.2322076>.
- [18] S.A. Vanalakar, P.S. Patil, J.H. Kim, Recent advances in synthesis of Cu₂FeSnS₄ materials for solar cell applications: a review, *Sol. Energy Mater. Sol. Cells* 182 (2018) 204–219, <https://doi.org/10.1016/j.solmat.2018.03.021>.
- [19] F.K. Konan, H.J.T. Nkuissi, B. Hartiti, Numerical simulations of highly efficient Cu₂FeSnS₄ (CFTS) based solar cells, *Int. J. Renew. Energy Resour.* 9 (2019) 1865–1872, <https://doi.org/10.20508/jrer.v9i4.9816.g7829>.
- [20] Y.H. Khattak, F. Baig, S. Ullah, B. Mari, S. Beg, H. Ullah, Numerical modeling baseline for high efficiency (Cu₂FeSnS₄) CFTS based thin film kesterite solar cell, *Optik (Stuttg.)* 164 (2018) 547–555, <https://doi.org/10.1016/j.jleo.2018.03.055>.
- [21] H.T. Ganem, A.N. Saleh, M.A. Kamil, Simulation and improvement of the efficiency of the CFTS solar cell using SCAPS-1D, *Karbala Int. J. Mod. Sci.* 8 (2022) 62–69, <https://doi.org/10.33640/2405-609X.3207>.
- [22] S. Varku, K.P. Pradhan, S. Routray, Performance limitation of Cu₂FeSnS₄ solar cell: understanding impact of density of defect states, *Opt. Mater. (Amst.)* 133 (2022) 112885, <https://doi.org/10.1016/j.optmat.2022.112885>.
- [23] S. Varku, S. Routray, K.P. Pradhan, Understanding the effect of interface trap states on electrical and optical performance of CFTS thin film solar cell. 2022 IEEE Reg. 10 Symp. TENSYMP 2022, 2022, pp. 12–14, <https://doi.org/10.1109/TENSYMP54529.2022.9864372>.
- [24] K.C. Devendra, D.K. Shah, M.S. Akhtar, M. Park, C.Y. Kim, O.B. Yang, B. Pant, Numerical investigation of graphene as a back surface field layer on the performance of cadmium telluride solar cell, *Molecules* 26 (2021) 1–10, <https://doi.org/10.3390/molecules26113275>.
- [25] S.A.A. Kazmi, A.D. Khan, A.D. Khan, A.Rauf, W. Farooq, M. Noman, H. Ali, Efficient materials for thin-film CdTe solar cell based on back surface field and distributed bragg reflector, *Appl. Phys. A Mater. Sci. Process.* 126 (2020), <https://doi.org/10.1007/s00339-019-3221-5>.
- [26] G.M. Arumugam, S.K. Karunakaran, C. Liu, C. Zhang, F. Guo, S. Wu, Y. Mai, Inorganic hole transport layers in inverted perovskite solar cells: a review, *Nano Sel.* 2 (2021) 1081–1116, <https://doi.org/10.1002/nano.202000200>.
- [27] A.C. Nkele, A.C. Nwanya, N.M. Shinde, S. Ezugwu, M. Maaza, J.S. Shaikh, F. I. Ezema, The use of nickel oxide as a hole transport material in perovskite solar cell configuration: achieving a high performance and stable device, *Int. J. Energy Res.* 44 (2020) 9839–9863, <https://doi.org/10.1002/er.5563>.
- [28] H. Son, B.S. Jeong, Optimization of the power conversion efficiency of CsPbI_xBr_{3-x}-Based perovskite photovoltaic solar cells using ZnO and NiOx as an inorganic charge transport layer, *Appl. Sci.* 12 (2022), <https://doi.org/10.3390/app12188987>.
- [29] C. Gong, H. Li, H. Wang, C. Zhang, Q. Zhuang, A. Wang, Z. Xu, W. Cai, R. Li, X. Li, Z. Zang, Silver coordination-induced n-doping of PCBM for stable and efficient inverted perovskite solar cells, *Nat. Commun.* 15 (2024) 1–10, <https://doi.org/10.1038/s41467-024-49395-7>.
- [30] C. Gong, H. Li, Z. Xu, Y. Li, H. Wang, Q. Zhuang, A. Wang, Z. Li, Z. Guo, C. Zhang, B. Wang, X. Li, Z. Zang, Efficient and stable inverted perovskite solar cells enabled by homogenized PCBM with enhanced electron transport, *Nat. Commun.* 15 (2024), <https://doi.org/10.1038/s41467-024-53283-5>.
- [31] A. Islam, S.Z. Haider, M. Wang, A.G. Ismail, H. Anwar, Interface engineering for improved performance of perovskite solar cells using CdTe buffer layer, *Results Eng.* 23 (2024), <https://doi.org/10.1016/j.rineng.2024.102618>.
- [32] N. Hunwick, X. Liu, M. Togay, J.M. Walls, P.J.M. Isherwood, The effect of oxygen on NiO as a back buffer layer in CdTe solar cells, *Energy Adv.* (2024) 1746–1753, <https://doi.org/10.1039/d4ya00125g>.
- [33] H. Search, C. Journals, A. Contact, M. Iopscience, I.P. Address, [26] (sputtering) JJAP.34.2440, 2440 (n.d.).
- [34] R. Ranjan, N. Anand, M.N. Tripathi, N. Srivastava, A.K. Sharma, M. Yoshimura, L. Chang, R.N. Tiwari, SCAPS study on the effect of various hole transport layer on highly efficient 31.86% eco-friendly CZTS based solar cell, *Sci. Rep.* 13 (2023) 1–16, <https://doi.org/10.1038/s41598-023-44845-6>.
- [35] S. Mansouri, L. Dehimi, H. Bencherif, F. Pezzimenti, M. Zulfiqar, N.H. Alotaibi, S. Mohammad, R. Haldhar, M.A. Darwish, M.K. Hossain, Theoretical simulation on enhancing the thin-film copper zinc tin sulfide solar cell performance using MoS₂, MoO_x, and CuI as efficient hole transport layers, *Energy Fuels* 38 (2024) 8187–8198, <https://doi.org/10.1021/acs.energyfuels.4c00200>.
- [36] M.K. Hossain, M.H.K. Rubel, G.F.I. Toki, I. Alam, M.F. Rahman, H. Bencherif, Effect of various electron and hole transport layers on the performance of CsPbI₃-Based perovskite solar cells: a numerical investigation in DFT, SCAPS-1D, and wxAMPS frameworks, *ACS Omega* 7 (2022) 43210–43230, <https://doi.org/10.1021/acsomega.2c05912>.
- [37] X. Li, D. Xiao, L. Wu, D. Wang, G. Wang, D. Wang, CdTe thin film solar cells with copper iodide as a back contact buffer layer, *Sol. Energy* 185 (2019) 324–332, <https://doi.org/10.1016/j.solener.2019.04.082>.
- [38] W. Sun, S. Ye, H. Rao, Y. Li, Z. Liu, L. Xiao, Z. Chen, Z. Bian, C. Huang, Room-temperature and solution-processed copper iodide as the hole transport layer for inverted planar perovskite solar cells, *Nanoscale* 8 (2016) 15954–15960, <https://doi.org/10.1039/c6nr04288k>.
- [39] X. Jia, L. Shen, Y. Liu, W. Yu, X. Gao, Y. Song, W. Guo, S. Ruan, W. Chen, Performance improvement of inverted polymer solar cells thermally evaporating CuI as an anode buffer layer, *Synth. Met.* 198 (2014) 1–5, <https://doi.org/10.1016/j.synthmet.2014.09.035>.
- [40] S. Yoon, H. Kim, E.Y. Shin, I.G. Bae, B. Park, Y.Y. Noh, I. Hwang, Enhanced hole extraction by interaction between CuI and MoO₃ in the hole transport layer of organic photovoltaic devices, *Org. Electron.* 32 (2016) 200–207, <https://doi.org/10.1016/j.orgel.2016.02.036>.
- [41] J. Just, C.M. Sutter-Fella, D. Lützenkirchen-Hecht, R. Frahm, S. Schorr, T. Unold, Secondary phases and their influence on the composition of the kesterite phase in CZTS and CZTSe thin films, *Phys. Chem. Chem. Phys.* 18 (2016) 15988–15994, <https://doi.org/10.1039/c6cp00178e>.
- [42] M. Kumar, A. Dubey, N. Adhikari, S. Venkatesan, Q. Qiao, Strategic review of secondary phases, defects and defect-complexes in kesterite CZTS-Se solar cells, *Energy Environ. Sci.* 8 (2015) 3134–3159, <https://doi.org/10.1039/c5ee02153g>.
- [43] M. Burgelman, K. Decock, A. Niemegeers, J. Verschraegen, S. Degreve, SCAPS manual, 1–111, University of Ghent: Ghent, Belgium, 2016.
- [44] B. Barman, S. Ingole, Analysis of Si Back-Contact for Chalcogenide Perovskite Solar Cells Based on BaZrS₃ Using SCAPS-1D, *Adv. Theory Simul.* 6 (2023), <https://doi.org/10.1002/adts.202000820>.
- [45] M.D. Wanda, S. Ouédraogo, F. Tchoffo, F. Zougmoré, J.M.B. Ndjaka, Numerical investigations and analysis of Cu₂ZnSnS₄ based solar cells by SCAPS-1D, *Int. J. Photoenergy* 2016 (2016), <https://doi.org/10.1155/2016/2152018>.
- [46] M.N.H. Riyad, A. Sunny, M.M. Khatun, S. Rahman, S.R. Al Ahmed, Performance evaluation of WS₂ as buffer and Sb2S₃ as hole transport layer in CZTS solar cell by numerical simulation, *Eng. Rep.* 5 (2023) 1–17, <https://doi.org/10.1002/eng.212600>.
- [47] N. Doumit, K. Soro, A. Ozocak, N. Batut, A. Schellmanns, E. Saintaime, E. Ntsoenzoek, Boosting the efficiency of CZTS/Si tandem solar cells using In₂O₃ layer in CZTS top cell, *Adv. Theory Simul.* 4 (2021) 1–7, <https://doi.org/10.1002/adts.202100099>.
- [48] Y.H. Khattak, F. Baig, S. Ullah, B. Mari, S. Beg, K. Khan, Effect of Cu₂O hole transport layer and improved minority carrier life time on the efficiency enhancement of Cu₂NiSnS₄ based experimental solar cell, *J. Renew. Sustain. Energy* 10 (2018), <https://doi.org/10.1063/1.5037471>.
- [49] H.T. Ganem, A.N. Saleh, Enhancement of the efficiency of the CZTS/Cds/Zno/ITO solar cell by back reflection and buffer layers using SCAPS-1D, *Iraqi J. Sci.* 62 (2021) 1144–1157, <https://doi.org/10.24996/ijss.2021.62.4.11>.
- [50] A. Haddout, A. Raidou, M. Fahoume, A review on the numerical modeling of CdS/CZTS-based solar cells, *Appl. Phys. A Mater. Sci. Process.* 125 (2019), <https://doi.org/10.1007/s00339-019-2413-3>.
- [51] D.A.R. Barkhouse, O. Gunawan, T. Gokmen, T.K. Todorov, D.B. Mitzi, Yield predictions for photovoltaic power plants: empirical validation, recent advances and remaining uncertainties, *Prog. Photovoltaics Res. Appl.* 20 (2015) 6–11, <https://doi.org/10.1002/pip>.
- [52] M. Jamil, M. Amami, A. Ali, K. Mahmood, N. Amin, Numerical modeling of AZTS as buffer layer in CZTS solar cells with back surface field for the improvement of cell performance, *Sol. Energy* 231 (2022) 41–46, <https://doi.org/10.1016/j.solener.2021.11.025>.
- [53] M.H. Azar, S. Aynehband, H. Abdollahi, H. Alimohammadi, *Photonics-10-00271-V2, Pdf*, 2023.
- [54] M.M. Salah, A. Zekry, A. Shaker, M. Abouelatta, M. Mousa, A. Saeed, Investigation of electron transport material-free Perovskite/CIGS tandem solar cell, *Energies* 15 (2022), <https://doi.org/10.3390/en15176326>.
- [55] Y. Nouri, B. Hartiti, A. Batan, H. Labrim, S. Fadili, P. Thévenin, Cu₂XSnS₄ (X = Mn, Fe, Co) semiconductors: boltzmann theory and DFT investigations, *Solid State Commun.* 339 (2021), <https://doi.org/10.1016/j.ssc.2021.114491>.
- [56] A. Kowsar, S.C. Debnath, M. Shafayet-Ul-Islam, M.J. Hossain, M. Hossain, A. K. Chowdhury, G. Hashmi, S.F.U. Farhad, An overview of solar cell simulation tools, *Sol. Energy Adv.* 5 (2025) 100077, <https://doi.org/10.1016/j.seja.2024.100077>.
- [57] R. Jayakrishnan, A. Raj, Photosensitivity reversal in solution-processed copper zinc tin sulphide/cadmium sulphide superstrate junction, *Thin Solid Films* 783 (2023) 140063, <https://doi.org/10.1016/j.tsf.2023.140063>.
- [58] H.J. Tchognia Nkuissi, L.L. Mambo Nguyeup, A. Dadje, G.M. Tchapga Gnamsi, A.C. Chéagé, B. Hartiti, J.M. Ndjaka, Effect of chemical and physical parameters on the electrical outputs of Cu₂Zn 1-y Fe y Sn₄-Based solar cells by wxAMPS, *Int. J. Photoenergy* 2020 (2020), <https://doi.org/10.1155/2020/8840411>.
- [59] R. Paul, S. Vallisree, T.R. Lenka, F.A. Talukdar, Modeling and simulation of CZTS thin-film solar cell for efficiency enhancement, *J. Electron. Mater.* 51 (2022) 2228–2235, <https://doi.org/10.1007/s11664-022-09449-2>.
- [60] M. Dey, M. Dey, T. Biswas, S. Alam, N.K. Das, M.A. Matin, N. Amin, Modeling of Cu₂ZnSnS₄ solar cells with bismuth sulphide as a potential buffer layer. 2016 5th Int. Conf. Informatics, Electron. Vision, ICIEV 2016, 2016, pp. 1095–1098, <https://doi.org/10.1109/ICIEV.2016.7760168>.
- [61] S.H. Zyoud, A.H. Zyoud, N.M. Ahmed, A.R. Prasad, S.N. Khan, A.F.I. Abdelkader, M. Shahwan, Numerical modeling of high conversion efficiency fto/zno/cds/czts/

- mo thin film-based solar cells: using scaps-1d software, Crystals (2021) 11, <https://doi.org/10.3390/cryst11121468>.
- [62] K. Sobayel, K.S. Rahman, M.R. Karim, M.O. Ajiaz, M.A. Dar, M.A. Shar, H. Misran, N. Amin, Numerical modeling on prospective buffer layers for tungsten di-sulfide (WS₂) solar cells by scaps-1D, chalcogenide, Lett 15 (2018) 307–315.
- [63] F. Belarbi, W. Rahal, D. Rached, S. benghabrit, M. Adnane, A comparative study of different buffer layers for CZTS solar cell using Scaps-1D simulation program, Optik 216 (2020) 164743, <https://doi.org/10.1016/j.jleo.2020.164743>.
- [64] M. Moustafa, Z. Abu Waar, S. Yasin, Optimizing solar performance of CFTSe-based solar cells using MoSe₂ as an innovative buffer layers, Sci. Rep. 15 (2025) 1–15, <https://doi.org/10.1038/s41598-024-82309-7>.
- [65] A.B. Coulibaly, S.O. Oyedele, N.R. Kre, B. Aka, Comparative study of lead-free perovskite solar cells using different hole transporter materials, Model. Numer. Simulat. Mater. Sci. 9 (2019) 97–107, <https://doi.org/10.4236/mnms.2019.94006>.
- [66] U. Mandadapu, S.V. Vedanayakam, K. Thyagarajan, M.R. Reddy, B.J. Babu, Design and simulation of high efficiency tin halide perovskite solar cell, Int. J. Renew. Energy Resour. 7 (2017) 1604–1612, <https://doi.org/10.20508/ijrer.v7i4.6182.g7270>.
- [67] J. Ray, T.K. Chaudhuri, C. Panchal, K. Patel, K. Patel, G. Bhatt, P. Suryavanshi, PbS-ZnO solar cell: a numerical simulation, J. Nano-Electron. Phys. 9 (2017), [https://doi.org/10.21272/jnep.9\(3\).03041](https://doi.org/10.21272/jnep.9(3).03041).
- [68] M. Fathi, M. Abderrezek, F. Djahli, M. Ayad, Study of thin film solar cells in high temperature condition, Study of thin film solar cells in high temperature condition, Energy Proc. 74 (2015) 1410–1417, <https://doi.org/10.1016/j.enpro.2015.07.788>.
- [69] E.M. Flores, R.A. Gouveia, M.J. Piotrowski, M.L. Moreira, Band alignment and charge transfer predictions of ZnO/ZnX (X = S, Se or Te) interfaces applied to solar cells: a PBE+ u theoretical study, Phys. Chem. Chem. Phys. 20 (2018) 4953–4961, <https://doi.org/10.1039/c7cp08177d>.
- [70] W. Lian, C. Jiang, Y. Yin, R. Tang, G. Li, L. Zhang, B. Che, T. Chen, Revealing composition and structure dependent deep-level defect in antimony trisulfide photovoltaics, Nat. Commun. 12 (2021) 1–7, <https://doi.org/10.1038/s41467-021-23592-0>.
- [71] K. Pandey, A.K. Patel, R. Mishra, Numerical study on performance enhancement of CZTSSe solar cells with Cu₂O and MoTe₂ as hole transport layer, J. Comput. Electron. 21 (2022) 895–904, <https://doi.org/10.1007/s10825-022-01900-1>.
- [72] O.K. Simya, A. Mahabobabatcha, K. Balachander, A comparative study on the performance of kesterite based thin film solar cells using SCAPS simulation program, Superlattice. Microst. 82 (2015) 248–261, <https://doi.org/10.1016/j.spmi.2015.02.020>.
- [73] M. Yousefi, M. Minbashi, Z. Monfared, N. Memarian, A. Hajjiah, Improving the efficiency of CZTSSe solar cells by engineering the lattice defects in the absorber layer, Sol. Energy 208 (2020) 884–893, <https://doi.org/10.1016/j.solener.2020.08.049>.
- [74] N. Touafek, R. Mahamdi, Excess defects at the CdS/CIGS interface solar cells, Chalcogenide Lett. 11 (2014) 589–596.
- [75] M. Minbashi, A. Ghobadi, E. Yazdani, A. Ahmadkhan Kordbacheh, A. Hajjiah, Efficiency enhancement of CZTSSe solar cells via screening the absorber layer by examining of different possible defects, Sci. Rep. 10 (2020) 1–14, <https://doi.org/10.1038/s41598-020-75686-2>.
- [76] A.S. Mathur, S. Dubey, Nidhi, B.P. Singh, Study of role of different defects on the performance of CZTSe solar cells using SCAPS, Optik (Stuttg) 206 (2020) 163245, <https://doi.org/10.1016/j.jleo.2019.163245>.
- [77] A. Redinger, S. Siebentritt, Loss mechanisms in kesterite solar cells, Copp. Zinc Tin Sulfide-Based Thin-Film Sol. Cells 627 (2015) 363–386, <https://doi.org/10.1002/9781118437865.ch16>.
- [78] M.K. Hossain, G.F.I. Toki, A. Kuddus, M.H.K. Rubel, M.M. Hossain, H. Bencherif, M.F. Rahman, M.R. Islam, M. Mushtaq, An extensive study on multiple ETL and HTL layers to design and simulation of high-performance lead-free CsSnCl₃-based perovskite solar cells, Sci. Rep. 13 (2023) 1–24, <https://doi.org/10.1038/s41598-023-28506-2>.
- [79] P.K. Kannan, M. Anandkumar, A theoretical investigation to boost the efficiency of CZTS solar cells using SCAPS-1D, Optik (Stuttg) 288 (2023) 171214, <https://doi.org/10.1016/j.jleo.2023.171214>.
- [80] M. Abdelfatah, W. Ismail, N.M. El-Shafai, A. El-Shaer, Effect of thickness, bandgap, and carrier concentration on the basic parameters of Cu₂O nanostructures photovoltaics: numerical simulation study, Mater. Technol. (2020) 1–9, <https://doi.org/10.1080/10667857.2020.1793092>.
- [81] G. Hodes, P.V. Kamat, Understanding the implication of carrier diffusion length in photovoltaic cells, J. Phys. Chem. Lett. 6 (2015) 4090–4092, <https://doi.org/10.1021/acs.jpclett.5b02052>.
- [82] A.S. Mathur, S. Dubey, Nidhi, B.P. Singh, Study of role of different defects on the performance of CZTSe solar cells using SCAPS, Optik (Stuttg) 206 (2020) 163245, <https://doi.org/10.1016/j.jleo.2019.163245>.
- [83] F. Baig, Y.H. Khattak, A. Shuja, K. Riaz, B.M. Soucase, Performance investigation of Sb₂Se₃ based solar cell by device optimization, band offset engineering and hole transport layer in SCAPS-1D, Curr. Appl. Phys. (2020), <https://doi.org/10.1016/j.cap.2020.06.005>.
- [84] S. Bansal, P. Aryal, Evaluation of New Materials for Electron and Hole Transport Layers in Perovskite-based Solar Cells Through SCAPS-1D Simulations, 2016, pp. 747–750.
- [85] S. Chen, J.H. Yang, X.G. Gong, A. Walsh, S.H. Wei, Intrinsic point defects and complexes in the quaternary kesterite semiconductor Cu₂ZnSnS₄, Phys. Rev. B Condens. Matter 81 (2010) 35–37, <https://doi.org/10.1103/PhysRevB.81.245204>.
- [86] G. Miceli, A. Pasquarello, Self-compensation due to point defects in Mg-doped GaN, Phys. Rev. B 93 (2016) 1–11, <https://doi.org/10.1103/PhysRevB.93.165207>.
- [87] M.A. Flores, W. Orellana, E. Menéndez-Proupin, Self-compensation in phosphorus-doped CdTe, Phys. Rev. B 96 (2017) 1–6, <https://doi.org/10.1103/PhysRevB.96.134115>.
- [88] L. Yin, G. Cheng, Y. Feng, Z. Li, C. Yang, X. Xiao, Limitation factors for the performance of kesterite Cu₂ZnSnS₄ thin film solar cells studied by defect characterization, RSC Adv. 5 (2015) 40369–40374, <https://doi.org/10.1039/c5ra00069f>.
- [89] D. Mora-Herrera, R. Silva-González, F.E. Cancino-Gordillo, M. Pal, Development of Cu₂ZnSnS₄ films from a non-toxic molecular precursor ink and theoretical investigation of device performance using experimental outcomes, Sol. Energy 199 (2020) 246–255, <https://doi.org/10.1016/j.solener.2020.01.077>.
- [90] Y.K. Liao, S.Y. Kuo, M.Y. Hsieh, F.I. Lai, M.H. Kao, S.J. Cheng, D.W. Chiou, T. P. Hsieh, H.C. Kuo, A look into the origin of shunt leakage current of Cu(In,Ga)Se₂ solar cells via experimental and simulation methods, Sol. Energy Mater. Sol. Cells 117 (2013) 145–151, <https://doi.org/10.1016/j.solmat.2013.05.031>.
- [91] M.A. Tashkandi, PINHOLES AND MORPHOLOGY OF CdS FILMS : the EFFECT ON THE OPEN Submitted by, 2012, pp. 1–152.
- [92] S.G. Kumar, K.S.R.K. Rao, Physics and chemistry of CdTe/CdS thin film heterojunction photovoltaic devices: fundamental and critical aspects, Energy Environ. Sci. 7 (2014) 45–102, <https://doi.org/10.1039/c3ee41981a>.
- [93] J.C. González, P.A. Fernandes, G.M. Ribeiro, A. Abelenda, E.R. Viana, P.M. P. Salomé, A.F. Da Cunha, Influence of the sulphurization time on the morphological, chemical, structural and electrical properties of Cu₂ZnSnS₄ polycrystalline thin films, Sol. Energy Mater. Sol. Cells 123 (2014) 58–64, <https://doi.org/10.1016/j.solmat.2014.01.005>.
- [94] S. Lee, E.S. Lee, T.Y. Kim, J.S. Cho, Y.J. Eo, J.H. Yun, A. Cho, Effect of annealing treatment on CdS/CIGS thin film solar cells depending on different CdS deposition temperatures, Sol. Energy Mater. Sol. Cells 141 (2015) 299–308, <https://doi.org/10.1016/j.solmat.2015.05.052>.
- [95] T.P. Weiss, I. Minguez-Bacho, E. Zuccalà, M. Melchiorre, N. Valle, B. El Adib, T. Yokosawa, E. Spiecker, J. Bachmann, P.J. Dale, S. Siebentritt, Post-deposition annealing and interfacial atomic layer deposition buffer layers of Sb₂Se₃/CdS stacks for reduced interface recombination and increased open-circuit voltages, Prog. Photovoltaics Res. Appl. 31 (2023) 203–219, <https://doi.org/10.1002/pip.3625>.
- [96] S.R. Biswal, D. Pradhan, A. Gartia, K.K. Sahoo, S. Sabat, J.P. Kar, Dependence of microstructure of thermally evaporated CuI films on the flow rate of argon gas, J. Mater. Eng. Perform. 33 (2024) 5331–5339, <https://doi.org/10.1007/s11665-023-08756-x>.
- [97] M. Zi, J. Li, Z. Zhang, X. Wang, J. Han, X. Yang, Z. Qiu, H. Gong, Z. Ji, B. Cao, Effect of deposition temperature on transparent conductive properties of γ -CuI film prepared by vacuum thermal evaporation, Phys. Status Solidi Appl. Mater. Sci. 212 (2015) 1466–1470, <https://doi.org/10.1002/pssa.20152015>.
- [98] B. Shi, J. Jia, X. Feng, G. Ma, Y. Wu, B. Cao, Thermal evaporated CuI film thickness-dependent performance of perovskite solar cells, Vacuum 187 (2021) 110076, <https://doi.org/10.1016/j.vacuum.2021.110076>.
- [99] S. Shi, J. Sun, J. Zhang, Y. Cao, A novel application of the CuI thin film for preparing thin copper nanowires, Phys. B Condens. Matter 362 (2005) 231–235, <https://doi.org/10.1016/j.physb.2005.02.019>.
- [100] C. Moditswe, C.M. Muiva, P. Luhanga, A. Juma, Effect of annealing temperature on structural and optoelectronic properties of γ -CuI thin films prepared by the thermal evaporation method, Ceram. Int. 43 (2017) 5121–5126, <https://doi.org/10.1016/j.ceramint.2017.01.026>.
- [101] D.K. Kaushik, M. Selvaraj, S. Ramu, A. Subrahmanyam, Thermal evaporated Copper Iodide (CuI) thin films: a note on the disorder evaluated through the temperature dependent electrical properties, Sol. Energy Mater. Sol. Cells 165 (2017) 52–58, <https://doi.org/10.1016/j.solmat.2017.02.030>.
- [102] L.K. Dintle, P.V.C. Luhanga, C. Moditswe, C.M. Muiva, Dependence of structural and optoelectronic properties on thickness of γ -cuI thin films deposited by vacuum thermal evaporation, MRS Adv. 3 (2018) 2627–2642, <https://doi.org/10.1557/adv.2018.317>.
- [103] Z.H. Li, J.X. He, X.H. Lv, L.F. Chi, K.O. Egbo, M. De Li, T. Tanaka, Q.X. Guo, K. M. Yu, C.P. Liu, Optoelectronic properties and ultrafast carrier dynamics of copper iodide thin films, Nat. Commun. 13 (2022), <https://doi.org/10.1038/s41467-022-34117-8>.
- [104] N.A. Mala, S. Sivakumar, K.M. Batoo, M. Hadi, Design and fabrication of iron-doped nickel oxide-based flexible electrode for high-performance energy storage applications, Inorg. Chem. Commun. 131 (2021) 14–19, <https://doi.org/10.1016/j.inoche.2021.108797>.
- [105] S. Saleem, A.H. Jabbar, M.H. Jameel, A. Rehman, Z.H. Kareem, A.H. Abbas, Z. Ghaffar, S.A. Razzaq, R.A. Pashameah, E. Alzahrani, E.P. Ng, S.M. Sapuan, Enhancement in structural, morphological, and optical properties of copper oxide for optoelectronic device applications, Nanotechnol. Rev. 11 (2022) 2827–2838, <https://doi.org/10.1515/ntrv-2022-0473>.